JGR Planets

RESEARCH ARTICLE
10.1029/2022JE007467

Determining Emplacement Conditions and Vent Locations for Channelized Lava Flows Southwest of Arsia Mons

I. T. W. Flynn[1], D. A. Crown[2], and M. S. Ramsey[1]

[1]Department of Geology and Environmental Science, University of Pittsburgh, Pittsburgh, PA, USA, [2]Planetary Science Institute, Tucson, AZ, USA

Key Points:

- Lava flows in the southwest flow field of Arsia Mons are not fully exposed, which hinders emplacement modeling based solely on the observable flow dimensions
- The total channelized flow length, effusion rate, viscosity, yield strength, and potential vent location for each flow are estimated using the PyFLOWGO model
- Four of the flows back-project upslope to a potential vent location examined in detail using context camera and mars orbiting laser altimeter data

Correspondence to:
I. T. W. Flynn,
itf2@pitt.edu

Citation:
Flynn, I. T. W., Crown, D. A., & Ramsey, M. S. (2022). Determining emplacement conditions and vent locations for channelized lava flows southwest of Arsia Mons. *Journal of Geophysical Research: Planets*, *127*, e2022JE007467. https://doi.org/10.1029/2022JE007467

Received 6 JUL 2022
Accepted 28 OCT 2022

Abstract The lava flow field southwest of Arsia Mons, Mars has complex volcanic geomorphology. Overlapping flows make observations of their total lengths and identification of their source vents impossible. Application of flow emplacement models, which rely upon physical parameters such as flow length, using only the exposed flow may produce inaccurate estimates of effusion rate, viscosity, and yield strength. We use an established terrestrial thermorheological model (PyFLOWGO), modified to Mars conditions, to estimate effusion rates, viscosities, yield strengths, and possible vent locations for five Mars flows. Our investigation found a range of effusion rates from 2,500 to 6,750 $m^3\ s^{-1}$ (average of ~4,960 $m^3\ s^{-1}$). These results are an order of magnitude higher than terrestrial channelized basaltic flows. Corresponding modeled viscosities and yield strengths ranged from 9.4×10^3 to 6.6×10^5 Pa s (average of 5.5×10^4 Pa s) and 66 to 381 Pa (average of 209 Pa), respectively. A novel secondary application of PyFLOWGO that assumes upslope channel narrowing provided estimates of the entire channel length, which is on average four times longer than the exposed portions. Projecting these lengths upslope shows that four of the five flows may have a common vent location, which shares morphologic similarities to other Tharsis region vents. This modeling approach for partially-exposed lava flows makes it possible to not only determine eruptive parameters, but also to estimate total channel lengths and thereby identify possible source vents.

Plain Language Summary Volcanism is a critical component of Mars' surface formation and evolution. Some of the most recent volcanic activity occurred southwest of Arsia Mons, a volcano in the Tharsis Volcanic Province. A major limitation for studying flows in this region and elsewhere on Mars is that the sources of these flows are not known because their upper/near-vent parts are commonly buried. We used a novel modeling application for five flows southwest of Arsia Mons to first estimate eruption and flow parameters (e.g., flow rate and viscosity) and then, a possible vent location. We measured flow dimensions (e.g., channel width and length) to corroborate model results. Modeled flow rates are approximately 10 times higher than estimated for large flows on Earth but are within the range of prior modeling results for Mars. Lava flow properties were similar to values for flows on Earth, but lower in comparison to past studies of Mars. We also identified a potential source for four of the five flows. These results show that the observed portion of a lava flow only represents a fraction of the total flow length, and that high flow rates are necessary to produce the long flow lengths on Mars.

1. Introduction

A channelized lava flow indicates specific emplacement conditions, which can be modeled to determine emplacement parameters such as effusion rate, flow duration, viscosity, and yield strength (e.g., Garry et al., 2007; Glaze & Baloga, 2006; Hiesinger et al., 2007; Hodges & Moore, 1994). Previous studies have investigated channelized flows on Mars at Ascraeus Mons, Pavonis Mons, and Arsia Mons (e.g., Baloga et al., 2003; Baloga & Glaze, 2008; Garry et al., 2007; Glaze et al., 2009; Hiesinger et al., 2007). These studies were limited, however, to modeling only the visibly exposed extent of a flow, as it is common for the proximal (i.e., near vent) portions of Martian lava flows to be covered by younger, overlapping flows or obscured by aeolian mantling deposits. Modeling the visible extent of a flow can provide useful insights into the emplacement mechanisms, but those results may contain significant error if the modeled results presuppose that the input flow length equals the total length.

Channelized lava flows are commonly observed across the major volcanic provinces on Mars. Many of these have well-developed central channels that can extend for over ten to hundreds of kilometers (Baloga et al., 2003; Carr et al., 1977; Mouginis-Mark & Yoshioka, 1998; Zimbelman, 1985, 1998). They have been studied at Ascraeus Mons, Olympus Mons, and Elysium Mons (e.g., Garry et al., 2007; Hiesinger et al., 2007; Hulme, 1976; Pasckert

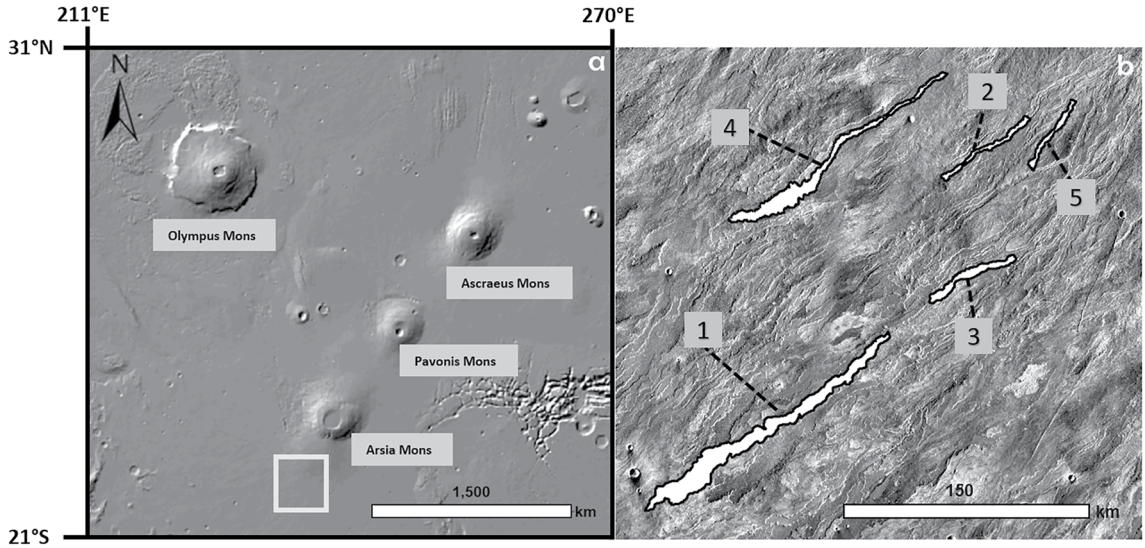

Figure 1. (a) Shaded relief image derived from the Mars Orbiter Laser Altimeter (MOLA)/ High Resolution Stereo Camera (HRSC) blended digital elevation model (DEM) data set (Fergason et al., 2018), showing the Tharsis Montes volcanic region and the study area, outlined by the white box (14°–20.5°S, 122.5°–128.4°E). There are ~21 lava flows with well defined central channels in the study area; we chose five representative flows based on size, areal distribution, and central channel development. (b) THEMIS daytime TIR mosaic with the five flows outlined and numbered.

et al., 2012; Wilson & Mouginis-Mark, 2001). Across the Tharsis Montes, Arsia Mons has some of the youngest and best-preserved channelized lava flows in the flow field southwest of the volcano (Crown & Ramsey, 2017). Detailed mapping of the region has not identified distinct vents associated with a particular flow or group of flows (Crown & Ramsey, 2017; Giacomini et al., 2012; Richardson et al., 2021).

Here we use the PyFLOWGO thermorheological model developed for terrestrial applications (Chevrel et al., 2018; Harris & Rowland, 2001) and modified for Martian conditions to determine the emplacement and flow parameters (e.g., the effusion rate, lava viscosity and yield strength) of a subset of the Arsia Mons channelized flows whose aerial extent is not completely visible. These results are compared to past studies that used different modeling approaches. Novel to this work is that we apply PyFLOWGO a second time to each of the flows to constrain channel width rather than exposed channel length. This provides the ability to estimate the total channel length (e.g., exposed + buried portions). We then project these channelized lengths back upslope to search for potential vent locations (Figure 1). An important caveat with the modeling method and results is that we constrain the model's rheologic and topographic inputs with a terrestrial analog and current Mars datasets (see Section 2.4 and 2.5). We do not explore the full range of plausible inputs, which would increase the uncertainty in the results presented.

1.1. Geologic Background

Arsia Mons is the southernmost of the Tharsis Montes (Figure 1a) with an elevation of 17.7 km, a diameter of 300 km, and flank slopes averaging ~5° (Greeley & Spudis, 1981; Plescia, 2004). The flanks and caldera floor are mostly composed of lava flows, which serve as the primary construction material (Mouginis-Mark & Rowland, 2008). Arsia Mons has a well-developed, single-collapse summit caldera with a volume of ~4,000 km^3 that has evidence of volcanism as recent as the last 150 Ma (Richardson et al., 2017). Emanating from the northeast and southwest flanks are two large flow field aprons, both of which postdate and surround the main edifice (Bleacher et al., 2007; Crumpler & Aubele, 1978; Garry et al., 2014; Scott & Zimbelman, 1995). The southwest flow apron expands into and forms Daedalia Planum to the south. The five flows investigated for this study are located in this region (Figure 1). This elevated plains region consists of overlapping lava flows emplaced during the Hesperian and Amazonian Periods and is sparsely cratered (Berman & Crown, 2019; Chuang et al., 2016; Scott & Tanaka, 1986; Tanaka et al., 2014). The regional slope decreases steadily from 5° along the base of Arsia Mons to ~0° at the southern margin of Daedalia Planum (Crown et al., 2012). Despite this region being composed of flows that display pahoehoe- and a'a-like end-members (Crown & Ramsey, 2017), volcanic vents have not been identified (Crown & Ramsey, 2017; Giacomini et al., 2012; Richardson et al., 2021). Flows in the region

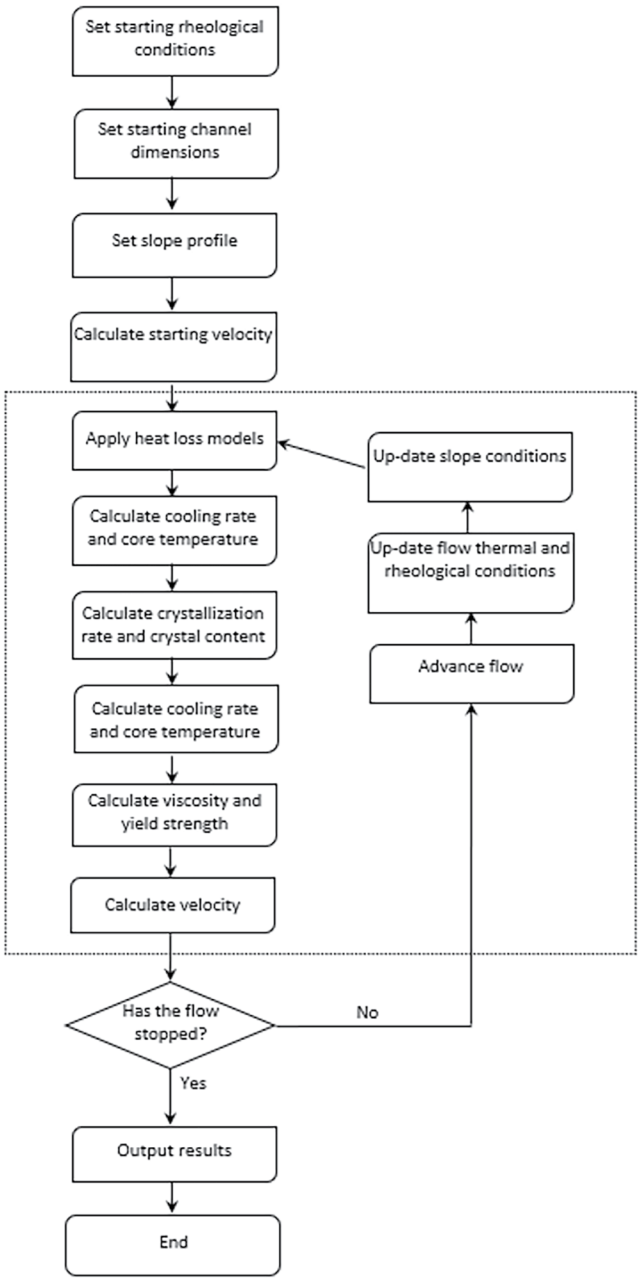

Figure 2. Workflow showing the main steps executed by the PyFLOWGO model (modified from Harris & Rowland, 2015). The region inside the dashed box indicates the model steps for calculating heat gain and loss. The calculations within the dashed box are repeated for each "step" of the model based on the chosen model step size until the flow has been assessed to stop. Stopping conditions for the flow are discussed in Section 2.1.

of 22.5°–27.5°S and 120°–130°W have estimated ages of only a few 100 Ma (Berman & Crown, 2019; Crown et al., 2015), indicating that they are some of the youngest on Mars. Using Visible and Infrared Mineralogical Mapping Spectrometer (OMEGA), Thermal Emission Imaging System (THEMIS) and Thermal Emission Spectrometer data, some lava flows in the Daedalia Planum were found to contain mafic minerals consistent with basaltic to tholeiitic basaltic composition (Giacomini et al., 2012; Lang et al., 2009). This conclusion is also consistent with findings for several Arsia Mons flows studied by Warner & Gregg (2003), who used physical parameters of the flows (e.g., flow dimensions, ridge spacing, and amplitude) to estimate rheological properties consistent with basaltic to basaltic andesite compositions.

2. Methods

2.1. PyFLOWGO

FLOWGO, originally described by Harris & Rowland (2001), is a self-adaptive, one-dimensional, analytical, thermorheological model applicable to channelized lava flows. It tracks the heat gains and losses of an element of lava flowing down a channel at a calculated (or known, for active flows) eruption rate. FLOWGO recalculates all heat-dependent terms that affect the lava cooling in each modeling step, using them to determine the lava advance rate down the channel (Figure 2). The heat losses are those due to radiation, convection, conduction, and vapourization of precipitation (if applicable). The heat gains are due to latent heat of crystallization and viscous dissipation. Heat loss from the modeled lava is dominated by radiative heat flux, which is a function of the temperature and effective emissivity of the lava's radiating surface, which consists of molten and crusted fractions (Ramsey et al., 2019; Rowland et al., 2004). Our analysis utilizes a new two-component emissivity adaptation incorporated in the model that accounts for the difference in emissivity between the exposed molten and cooler crusted surfaces. This has been shown to reproduce the emplaced flow length of an active basaltic lava flow more accurately than a single emissivity assumption (Ramsey et al., 2019).

The original FLOWGO model was recoded and updated in the Python coding language to PyFLOWGO, which allows for improved iteration and customization including the choice of viscosity modules (Chevrel et al., 2018). The governing equation of the PyFLOWGO model continues to be the Jeffrey's equation for a Newtonian flow in an open channel, modified for a Bingham fluid, to determine the mean velocity (V_c) of the lava in the channel:

$$V_c = \left(\frac{d^2 \rho_{\text{lava}} g \sin \emptyset}{3\eta_{\text{lava}}}\right)\left[1 - \left(\frac{3}{2}\right)\left(\frac{\text{YS}_{\text{core}}}{\text{T}_{\text{base-of-core}}}\right) + \left(\frac{1}{2}\right)\left(\frac{\text{YS}_{\text{core}}}{\text{T}_{\text{base-of-core}}}\right)^3\right] \quad (1)$$

In Equation 1, YS_{core} is the yield strength of the fluid core, $\text{T}_{\text{base-of-core}}$ is the amount of shear stress required to deform the lava at the base of the flow's core, ρ_{lava} is lava density, η_{lava} is the dynamic viscosity, d is the channel depth, $\emptyset$ is the slope, and g is the acceleration due to gravity. Viscosity is determined by the choice of one of several internal viscosity modules available to the user. Setting the yield strength to zero reduces the equation to the original form of the Jeffrey's equation.

As with any lava flow model, PyFLOWGO relies upon several assumptions, which include: (a) the lava flow velocity is defined by the initial effusion rate at the head of the channel with a measured depth and width (for an older flow) or the effusion rate is calculated directly for an active flow using one of several approaches; (b) the

flowing lava must be confined to an open-channel with no continuous roofing or tube formation; (c) the vertical thermal structure of the lava is divided into three layers: a cooler basal crust, a homogeneous high-temperature molten core, and a radiating upper surface; (d) the model only simulates the propagation of channel-confined lava unhindered by the flow front or levee formation; and (e) the flow is cooling- rather than supply-limited, with stopping conditions governed by one of several aspects of flow cooling. PyFLOWGO also has limitations including: (a) it is unable to account for lava flow blockages/dams; (b) variable effusion rates; and (c) pahoehoe style flow emplacement (see Discussion for further details).

Before initiating a PyFLOWGO model run, the starting parameters and choice of an internal viscosity module are required (Figure 2). User-defined starting parameters (e.g., eruption temperature, viscosity, crystal fraction, vesicle fraction) are entered to set the starting rheology and are typically based on data from known and well-documented terrestrial flows, for example, Other physical parameters entered at the start include the initial channel width and depth, the heat loss parameters (e.g., emissivity of the crust and molten lava, starting crust cover fraction and temperature), environmental conditions (e.g., wind speed, ambient atmospheric temperature, density, and specific heat capacity), the model propagation step size, and finally, the slope profile of an existing flow (or that ahead of an actively-propagating flow). Numerous internal modules are included in PyFLOWGO to determine flow-dependent parameters such as: viscosity (melt and relative), yield strength, crystallization rate, vesicle fraction, effective crust cover, and crust temperature. For a full list of model options for PyFLOWGO see Chevrel et al. (2018) and references therein. Where applying PyFLOWGO to a planetary environment, some of the rheological and heat loss parameters are further constrained using a terrestrial analog (described in Section 2.3).

PyFLOWGO has three main stages: (a) determine the velocity of the lava at each new propagation step based on Equation 1; (b) calculate the total heat loss from the lava during each propagation step along the slope profile; and (c) determine the change in thermorheological conditions at each propagation step (Figure 2) (Harris & Rowland, 2001, 2015).

As a cooling-limited flow slows down because of cooling and increasing viscosity, it spreads laterally, commonly marking the end of the central channel, and will stop after it has cooled to an extent that its rheological behavior impedes forward motion (Chevrel et al., 2018). In contrast, a supply-limited flow lacks the down flow trend of increasing cooling rate and viscosity. Lava arrives at the flow front still relatively hot and with a lower viscosity commonly resulting in a complex morphology due to breakouts from the stalled front (Rhéty et al., 2017). In practice, PyFLOWGO has one of three stopping conditions: (a) the modeled velocity reaches zero; (b) the modeled temperature of the flow core reaches the point of solidus; (c) the modeled yield strength of the flow core increases such that the flow is unable to advance.

2.2. Previous Modeling Efforts

Many previous studies have investigated the emplacement of Martian lava flows primarily using fluid mechanics, wax analog experiments, various analytical and numerical models, as well as detailed flow measurements (e.g., Baloga & Glaze, 2008; Cattermole, 1987; Glaze & Baloga, 2006; Glaze et al., 2009; Griffiths & Fink, 1992; Hauber et al., 2011; Hiesinger et al., 2007; Hulme, 1976; Peters et al., 2021; Wechsler & Kroll, 2006). A common methodology for investigating Martian lava flows involves using the Graetz number to determine an effusion rate, which is then used with the modified Jeffrey's equation to determine viscosity (Hiesinger et al., 2007; Pasckert et al., 2012; Peters et al., 2021; Vaucher et al., 2009). The Graetz number, originally described for application to lava flows by Wilson & Head (1983) and later by Zimbelman (1985), is a dimensionless number that characterizes laminar flow in a conduit. It can be used to relate the rate of heat loss from a flow to the rate of heat advection within a flow along its length (Gregg & Fink, 1996). To use the Jeffrey's equation/Graetz number approach, measurements of flow length, width, and height are required, as well as a knowledge or assumption of a constant thermal diffusivity value. The Jeffrey's equation can be modified to derive viscosity if the appropriate inputs are known (e.g., effusion rate, density of the lava, and flow dimensions). Peters et al. (2021) demonstrated how uncertainty in the Graetz number produces a large range of calculated effusion rate and viscosity values. Recent work has also highlighted how ranges in the measured slope values can impact the outputs of the standard rheologic method (Russo et al., 2022). Furthermore, although this methodology has been widely used, it does not account for any heat loss variations due to the atmospheric conditions, lava composition or temperature, nor the rheological evolution of a flow as it advances, local topography, or the complex geometries of typical lava flows. Finally, and relevant to this work, all past studies only investigated the visible portion of a flow. Particularly in

this region of Arsia Mons, the observed flow lengths likely represent only a small fraction of the actual length. Therefore, any modeled effusion rates and rheologic parameters based only on these exposed lengths may misrepresent the true flow conditions at the time of emplacement.

2.3. Application of PyFLOWGO to Mars

PyFLOWGO can either be applied to active channelized flows in a predictive approach to model the eventual or observed channel length (e.g., Harris et al., 2019; Ramsey et al., 2019; Rowland et al., 2005; Thompson & Ramsey, 2021), or applied to older flows using detailed measurements of their lengths and central channel dimensions to estimate the eruptive conditions needed to create the flows (e.g., Beauchamp, 2017; Ramsey et al., 2019; Rowland et al., 2002). In addition to these measurements, the starting thermorheological and surface thermal structure conditions are necessary and typically provided using an analog flow. Prior studies have adapted the original FLOWGO model for Martian environmental conditions and applied it to lava flows in several locations on Mars (e.g., Beauchamp, 2017; Rowland et al., 2002, 2004). The adaptation of PyFLOWGO to Mars for this study follows the methods described in Rowland et al. (2002, 2004) by changing the gravity, ambient atmospheric temperature, and atmospheric composition (Table 1). The methods used here differ from Rowland et al. (2002, 2004), however, through the following improvements: (a) utilization of the two-component emissivity model for radiative cooling of the upper surface following the approach of Ramsey et al. (2019); (b) use of a colder lava surface crust temperature (625 vs. 823 K) because of the colder ambient atmospheric temperature (~210 K) following the approach of Beauchamp (2017); and (c) assuming that a greater percent of insulating crust formed across the flow surface (also due to the colder ambient atmospheric temperature). From here, modeling of individual flows is accomplished in a two-step procedure as done in Rowland et al. (2002). Two of the multiple outputs of PyFLOWGO (modeled channel length and modeled channel width) are used to fit the actual flows, whose measured channel dimensions can corroborate the model results.

The initial application of the model here focuses only on the visible section of a channelized flow. A typical PyFLOWGO model run begins with certain assumptions and choices of internal modules (Table 1). The baseline for the model's input parameters is established using a terrestrial analog (in our case, the Tolbachik 2012–2013 eruption) (Table 1). Only three input parameters (eruption temperature, starting crystal fraction, and crystals grown during cooling) are iteratively refined, within plausible limits, to best fit the exposed channel length (Table 1). These three parameters were chosen to keep model integrity in regards to the Tolbachik analog flow and because they are variable in the literature (Plechov et al., 2015). The iterative fitting of the exposed channelized flow length is considered complete once the modeled channel length matches the observed channelized flow length to <5%. Matching the observed channel length to <5% is a higher accuracy requirement than prior terrestrial applications of the model (Rowland et al., 2005). The primary result of this step is to determine an effusion rate necessary to produce the exposed channel length. The modeled effusion rate is then used in a second application of PyFLOWGO to determine the total channelized flow length by constraining the observed channel width rather than the channelized flow length. Only flows that have an observable channel terminus can be used in this modeling. Consistent with previous applications of PyFLOWGO to Martian lava flows (i.e., Rowland et al., 2002, 2004) a constant slope of 2° is used for all modeling (see Discussion for further details).

Using the calculated effusion rate and rheologic variables from Step 1, the second application of the model runs iteratively, narrowing the initial channel width upslope for each model run (Tables 2 and 3). This approach assumes channel narrowing the closer it is to the source and is based on observed channelized lava flows on both Earth and Mars (Cashman et al., 2013; Dietterich & Cashman, 2014; Peitersen & Crown, 1999). Here, we assume the channel exists all the way back to the source from the first downflow location where the channel is seen in the images. Lava flows with channels present from their sources to their distal ends after the eruption has ceased are observed on Earth (e.g., Ganci et al., 2020; Ramsey et al., 2019) but have not been seen in the southwest (SW) Arsia Mons flow field. The PyFLOWGO second stage modeling step is considered complete once the measured final channel width matches the modeled channel width to <5%. The final channel width is determined at the last location that the central channel is visible. The results of this modeling yield an estimated total channel length, in addition to the flow's core temperature, viscosity, yield strength, mean velocity, and crust fraction during formation.

Once the modeled total channel length is determined, it is projected back upslope, following the regional aspect (slope direction) and generated slope vectors. The regional aspect and slope vectors upslope from each flow are calculated from the mars orbiting laser altimeter (MOLA)/high resolution stereo camera (HRSC) (~200 m/pixel;

Table 1
All PyFLOWGO Input Models and Parameters That Were Used for the Martian Lava Flow Modeling

	Units	Tolbachik	Mars	Mars best fit	
Module name					
Crystallization rate model		Basic	Basic	Basic	Harris and Rowland (2001) and Chevrel et al. (2018)
Melt viscosity model		VFT	VFT	VFT	Giordano et al. (2008)
Relative viscosity model		ER	ER	ER	Einstein-Roscoe (ER) model from Chevrel et al. (2018)
Yield strength model		Ryerson	Ryerson	Ryerson	Ryerson et al. (1988)
Crust temperature model		Constant	Constant	Constant	Harris and Rowland (2001) and Chevrel et al. (2018)
Effective crust cover model		Basic	Basic	Basic	Harris and Rowland (2001) and Chevrel et al. (2018)
Vesicle fraction model		Constant	Constant	Constant	Harris and Rowland (2001) and Chevrel et al. (2018)
Measured Parameters					
Starting channel width	m	30	Measured for each flow		Measured from CTX
Starting channel depth	m	6.1	Measured for each flow		Measured from MOLA PEDR
Average slope	°	2	2	2	Measured from MOLA/HRSC DEM
Variable parameters					
eruption temperature	K	1,355.15	1,355.15	1,300.15 to 1,355.15	Ramsey et al. (2019) and this study
crystal fraction		0.25	0.25	0 to 0.25	Ramsey et al. (2019) and this study
crystals grown during cooling		0.37	0.37	0.2 to 0.37	Ramsey et al. (2019) and this study
effusion rate	m^3/s	278	Different for each flow		Ramsey et al. (2019)
Fixed Parameters					
Step size	m	10	50		Harris and Rowland (2001), Chevrel et al. (2018), and this study
gravity	m/s^2	9.81	3.7	3.7	
Lava state					
density dre	kg/m^3	2,630	2,630	2,630	Ramsey et al. (2019)
vesicle fraction		0.06	0.06	0.06	Ramsey et al. (2019)
Radiation parameters					
Stefan-Boltzmann sigma	$W/m^2/K^4$	5.67E−08	5.67E−08	5.67E−08	Ramsey et al. (2019)
emissivity epsilon crust		0.95	0.95	0.95	Ramsey et al. (2019)
emissivity epsilon uncrusted		0.6	0.6	0.6	Lee and Ramsey (2016) and Ramsey et al. (2019)
Conduction parameters					
basal temperature	K	773.15	773.15	773.15	Ramsey et al. (2019)
core base distance		19	19	19	Ramsey et al. (2019)
Convection parameters					
wind speed	m/s	5	5	5	Ramsey et al. (2019)
wind friction factor		0.0036	0.0036	0.0036	Ramsey et al. (2019)
air temperature	K	273.15	210.15	210.15	Ramsey et al. (2019) and this study
air density	kg/m^3	0.4412	0.0212	0.0212	Ramsey et al. (2019) and this study
air specific heat capacity	J/kg × K	1,099	860	860	Ramsey et al. (2019) and this study
Thermal parameters					
buffer	°C	140	140	140	Harris and Rowland (2001)
crust cover fraction		0.9	0.9	1	Ramsey et al. (2019) and this study
alpha		−0.16	−0.16	−0.00756	Ramsey et al. (2019) and this study
crust temperature	°C	773.15	773.15	625.15	Ramsey et al. (2019) and this study
Melt viscosity parameters					

Table 1
Continued

	Units	Tolbachik	Mars	Mars best fit	
a_vft	Pa s	−4.55	−4.55	−4.55	Volynets et al. (2015)
b_vft	J/mol	6,887.303	6,887.303	6,887.303	Volynets et al. (2015)
c_vft	K	527.44	527.44	527.44	Volynets et al. (2015)
Crystal parameters					
solid temperature	K	1,253.15	1,253.15	1,253.15	Ramsey et al. (2019)
latent heat of crystallization	J/kg	350,000	350,000	350,000	Harris and Rowland (2001) and Chevrel et al. (2018)

Note. For a full breakdown of abbreviations in the table see Chevrel et al. (2018).

±3 m vertical resolution) blended digital elevation model (DEM) using the standard tools in ArcGIS (Fergason et al., 2018). The back projected channel lengths are used to search for potential vents using visible data from the context camera (CTX) and topographic analysis from the MOLA/HRSC DEM.

PyFLOWGO calculates heat loss and rheologic parameters for a well-established channelized lava flow. This does not include the zone of shear and dispersed flow that extends beyond the channel. For terrestrial flows this may be a region of <1–2 km within a multiple kilometer to tens of kilometers long flow (Dietterich & Cashman, 2014; Lipman & Banks, 1987). For Martian lava flows this dispersed zone can extend for a few kilometers or up to 50 km and comprise anywhere between 5% and 24% of the observable flow length (Table 2).

2.4. PyFLOWGO Initiation

A combination of terrestrial analog measurements from an active basaltic lava flow and detailed flow measurements for the five Arsia Mons flows were used to apply and constrain PyFLOWGO under Martian conditions. Using an analog data set is consistent with previous applications of FLOWGO to Mars (Beauchamp, 2017; Rowland et al., 2002, 2004), where rheological parameters from the 1984 Mauna Loa lava flow (Rowland et al., 2002, 2004) or the 2010 Piton de la Fournaise flow (Beauchamp, 2017) were used. Here, the 2012–2013 eruption of the Tolbachik volcanic complex (Russia) is used. This eruption and its lava flows make a compelling analog for three reasons: (a) they are compositionally similar (basaltic trachyandesite) to prior studies of Mars igneous rocks (Filiberto, 2017; Sautter et al., 2015); (b) the largest (Leningradskoye) flow shares similar morphological characteristics (a large, long channelized flow with well-defined lateral levees), and preexisting topography (having a constant low slope) to those flows observed in the southwest Arsia Mons flow field; and (c) the eruption was investigated previously using an array of remote sensing datasets acquired during the Leningradskoye flow emplacement to constrain the PyFLOWGO results. The necessary rheological variables have been further constrained through a combination of remote sensing, field data, and laboratory sample analysis (Ramsey et al., 2019). Using an established, previously investigated, terrestrial analog for PyFLOWGO greatly improves the accuracy and iterative run time. We also use the same internal PyFLOWGO module choices as the Ramsey et al. (2019) study for the crystallization rate, melt viscosity, relative viscosity, yield strength, crust temperature, effective crust cover, and vesicle fraction (Table 1).

Previous eruptions that produced large open channel flows such as the 1984 eruption of Mauna Loa or the 2007 eruption of Kliuchevskoi are not as suitable for modeling the flows in our study region because they were emplaced on much steeper constant slopes (~5° and ~27°, respectively) as compared to the much lower (~0°–2°) slopes of the Arsia Mons flow field. Finally, because of the numerous flows present in the SW Arsia Mons flow field, the exact pre-flow topography of the underlying surface is not known. Therefore, we assume that the pre-flow topography is similar to the current average flow field and upslope topography of these flows (see Discussion for further details). Slope values are calculated from the MOLA/HRSC DEM in ArcGIS.

2.5. Flow Observations and Measurements

Initial identification of five channelized lava flows in the study region was made using the thermal infrared (TIR) mosaic (~100 m/pixel) created from THEMIS nighttime data (Christensen et al., 2004). Channelized lava flows

Table 2
Characteristics of Five Arsia Mons Flows Determined Using CTX Data for Flow Lengths (Observed) and Widths, and MOLA PEDR Data for Channel Depths

	# of channel width measurements	Measured total flow length (km)	Channel (%)	Starting channel width (m)	Final channel width (m)	Average channel width (m)	Median channel width (m)	Starting channel depth (m)
Flow 1	128	176	72.3	460	3,479	1,022 ± 73	635	31
Flow 2	61	64	93.7	784	1,127	738 ± 29	713	77
Flow 3	53	55	94.6	316	4,303	1,175 ± 105	923	48
Flow 4	128	152	83.6	279	3,627	1,129 ± 67	896	26
Flow 5	45	47	93.6	1,180	1,508	1,047 ± 42	1,008	28

commonly exhibit a distinctive pattern in the TIR nighttime images due to the presumed infilling of their central channels by fine-grained, low thermal inertia eolian material. This fine-grained fill shows a clear temperature difference compared to the rocky, higher thermal inertia flow levees (Simurda et al., 2019). Detailed flow measurements required for the PyFLOWGO modeling were made using (~6 m/pixel) CTX data (Malin et al., 2007). CTX also provides sufficient spatial coverage to allow the detailed flow measurements of the channel and flow widths to be made along the entire observable flow as well as characterize the surface morphology of the flows.

For each flow investigated, the flow margins were digitized and central channel width measurements made every 1,000 m along the channel length in ArcGIS using the CTX data (Figure 3d) for later comparison to the modeled channel widths. The central channel is defined here as the region between two identifiable levees. This comparison follows from previous terrestrial lava flow investigations that used PyFLOWGO (e.g., Chevrel et al., 2018; Ramsey et al., 2019). Total flow width measurements were also made every 1,000 m. Finally, to apply PyFLOWGO to an inactive lava flow, the starting channel width and depth are required. Ideally, these channel dimensions are made at/near to the vent. Because this location is not visible, the measurements are taken at the first location that the channel is seen. These measurements provide a starting flux rate from which the model propagates the flow down the channel. To calculate the starting channel depth, MOLA Precision Experiment Data Point Records (PEDR) data (~160 m spot size, ~300 m along track spacing and 37 cm effective vertical resolution) were used (Figures 3b and 3c). Channel depth estimates were made as close as possible to where the central channel is first visible in the CTX data. This location is referred to as the "starting channel depth" throughout the rest of the manuscript. PEDR data were taken perpendicular to the lava flow's central channel and were averaged together to determine the height of the channel and surrounding surfaces. The local elevation is calculated by averaging the PEDR points on either side of the flow as a proxy for the preexisting topography. The number of PEDR points used for the preexisting topography depends upon the space available between adjacent lava flows. The starting channel depth is then determined by subtracting these two measurements. Channel depth measurements are not performed down flow because PyFLOWGO holds the channel depth constant accounting

Table 3
Comparison of the Measured Channel Flow Length and Width to the Best Fit Model Results

	Measured channel length (km)	Modeled channel length (km)	Visible channel length (%)	Starting channel width (m)[a]	Modeled starting width (m)[b]	Width change downslope (%)[c]	Measured median slope (°)
Flow 1	127	530	24.2	460	110	76.1	0.18
Flow 2	60	417	13.2	784	110	86.0	0.45
Flow 3	52	124	47.6	316	135	57.3	0.43
Flow 4	127	524	24.3	279	65	76.7	0.36
Flow 5	44	319	13.8	1,180	160	86.4	0.35

Note. Slope for each flow was determine using MOLA/HRSC profiles.
[a]Measured at upslope location where channel is first identified in image data. [b]At vent location, predicted by matching final channel width. [c]Channel width change from where the channel is first visible upslope to last visible channel location downslope.

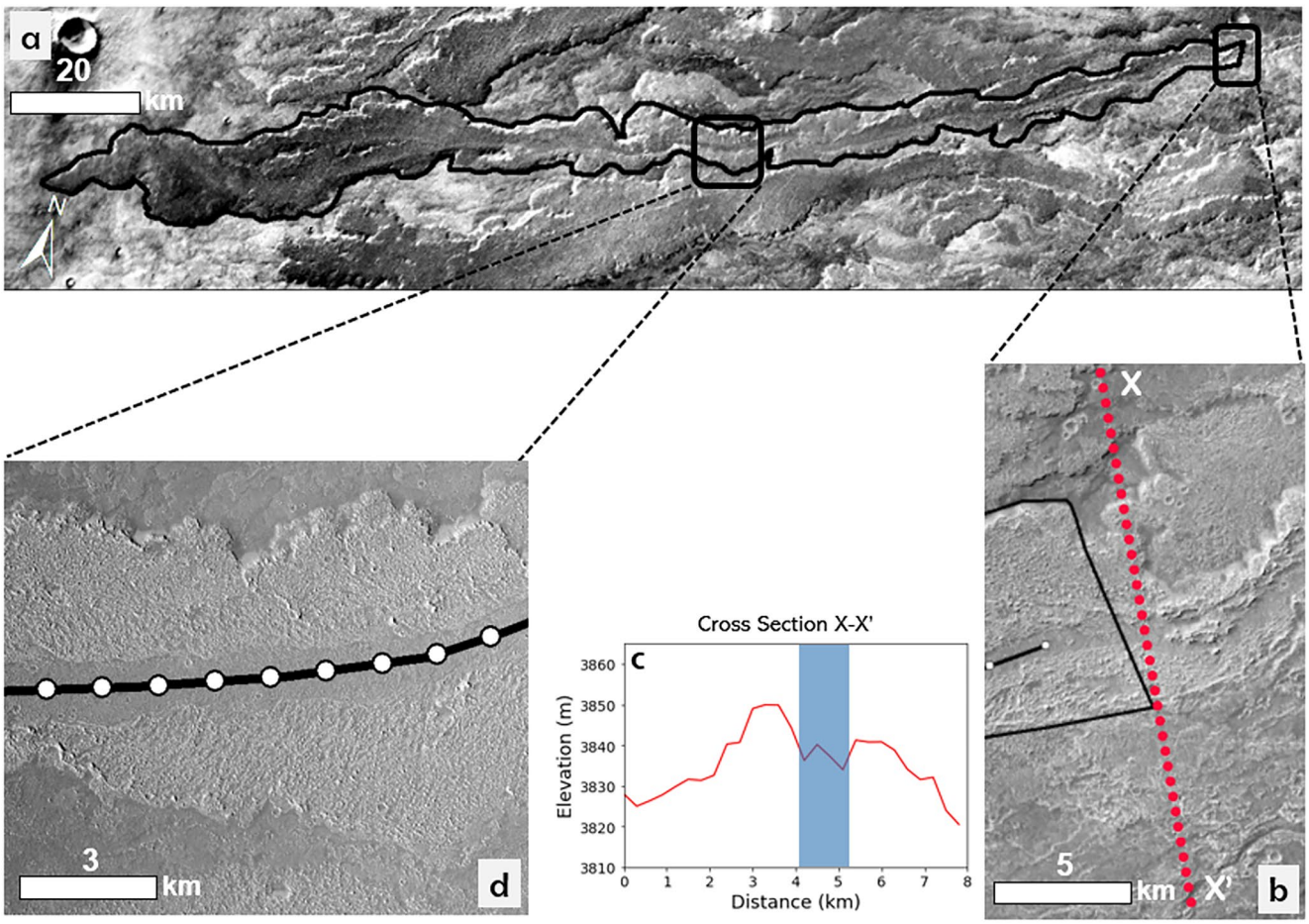

Figure 3. (a) THEMIS daytime TIR mosaic showing Flow 1 outlined in black. (b) Context camera (CTX) image (G15_024125_1596) of the exposed channel and levees. The red dots show the MOLA PEDR data used to calculate initial channel depth. Black line with white dots indicates the starting location of the central channel width measurements. (c) Cross-sectional profile derived from the MOLA data. The blue shading indicates the width of the central channel. (d) CTX image (P08_004188_1622) of Flow 1 further downflow highlighting the well-defined central channel and levees. White dots, spaced at 1000 m intervals, indicate where channel width measurements were made.

for changes in modeled velocity by varying the channel width. A nearly uniform channel depth along the length of the flow is consistent with many terrestrial observations (Lipman & Banks, 1987). The observable flow and channel length are also measured (Tables 2 and 3), but the modeled portion of the flow is limited to where the central channel is visible.

3. Results

The Mars-modified version of PyFLOWGO was applied to the five selected flows in the southwest Arsia Mons flow field (Figure 1). These flows were chosen because they are representative of the many channelized lava flows in the study region covering the range of lengths, visible morphologies, and amount of exposure. From the measurements and application of the PyFLOWGO model, the effusion rates were first determined. Next, the measured channel widths were compared to the results from the second application of PyFLOWGO to assess the accuracy of the model. Finally, the modeled channel length for the entire flow was projected upslope to a potential source location. Four of five flows appear to be part of a discrete flow field associated with a potential vent location that we investigate further.

3.1. Flow Descriptions

CTX images were used to identify morphologies and measure various properties of the central channel (where visible) for each flow. A Pearson Correlation coefficient was used to assess any relationship between the measured central channel width and the total flow width.

The five flows are all elongate, sinuous and can generally be broken into two groups, "short" flows (Flows 2, 3, and 5) and "long" flows (Flows 1 and 4). The central channel texture varies from knobby to darker and less rugged. At the distal end of the flows, the channels are lost where the flows spread laterally into broad lobes. All flows in CTX images have rugged surfaces with a higher albedo than the surrounding terrain. Each shares the same characteristics as the "bright, rugged flows" described in Crown and Ramsey (2017). The flow morphology and rugged upper surfaces are also similar to the flows investigated by Hiesinger et al. (2007) at Ascraeus Mons. Hiesinger et al. (2007) and Zimbelman and McAllister (1985) proposed that these are a'a flows. Based on the CTX observations of the flows at Arsia Mons and lacking small-scale flow morphological descriptions, we continue to use the "a'a-like" terminology of Crown and Ramsey (2017) for these flows. Below are more detailed descriptions and measurements for each flow.

Flow 1 (*long*): This flow has significant variations in total flow width along its length, possibly due to irregular pre-flow topography (Figure 4). The total exposed flow length is 176 km with a central channel observed for 127 km. Over the exposed length, the width of the channel increases downflow at an average rate of 23.7 m/1,000 m. The change in channel width does not follow a linear progression and is more similar to an exponential function. The observable extent of Flow 1 covers an area of 1,370 km^2. For comparison, the 2012–2013 Tolbachik eruption produced a flow field of ∼36 km^2 and the 2018 Kilauea eruption flow field covered ∼10 km^2 (Dietterich et al., 2021; Kubanek et al., 2017). Flow margins have two scales of sinuosity: one due to variable levee development and the other (smaller scale) due to spreading of individual lateral lobes (Figure 4c). In some locations, there appear to be multiple generations of lateral flow growth and levee emplacement. Flow margins are well defined along much of the extent of the flow but the flow is also buried or partly embayed in some locations by adjacent flows. The lateral margins of the flow exhibit knobby to ridged textures and are noticeably more rugged than channel surfaces. The channel is well defined over 72% of the flow length. The surface of the channel is darker and less rugged than the surrounding flow surface and is less sinuous than channels in the short flow category. The boundary between the channel and flow surface changes in ruggedness and albedo, whereas in other locations, it is denoted by linear ridges or troughs. In some locations, the linear features and flow textures suggest that the channel may have narrowed over the duration of the flow. Channel obstructions (potentially solidified lava blocks rafted downstream) are observed in a few locations but are less common than in the "short" flows. These features have the appearance of islands and are referred to as such throughout the rest of the manuscript. The channel widens significantly near the flow terminus, where the flow appears to exhibit some minor branching (i.e., lateral pulses of lava extend downslope) (Figure 4d).

Flow 2 (*short*): The central channel is defined for 60 km of the flow's 61 km observable length. Both the total flow width and central channel width are fairly uniform with fluctuations due to variable lateral spreading of levees (Figure 5b). The rate of channel width increase downflow is less than that of Flow 1 at 5.7 m/1,000 m and more variable. The exposed flow has an area of 186 km^2. The channel morphology, definition, and width vary noticeably. Some channel segments are sinuous (i.e., up-flow) but most are relatively straight with distinct depressed surfaces relative to the adjacent levees. Small islands are present within the central channel in many locations (Figure 5c). Channel definition gradually declines toward the flow terminus where a broad flow front is observed. Both the flow surface and levees are knobby at small-scales with the levees having slightly larger and more prominent ruggedness with some alignment of the knobs.

Flow 3 (*short*): Flow 3 is similar to Flow 2 in morphology and texture (Figure 6). The measured flow length is 55 km, with the central channel visible for 52 km, and a flow area of 245 km^2. A difference between the two flows is the variability in channel widening downflow (76.6 m/1000 m) (Figure 6b). The rate of channel growth follows a similar exponential trend to that of Flow 1. The central channel has a more distinct linear to curvilinear boundary with lateral levees over much of its length and has a more clearly lowered surface relative to the levees. This change in levee structure becomes clear toward the end of flow (Figure 6d). Several elongated islands are present in the central channel (Figure 6c).

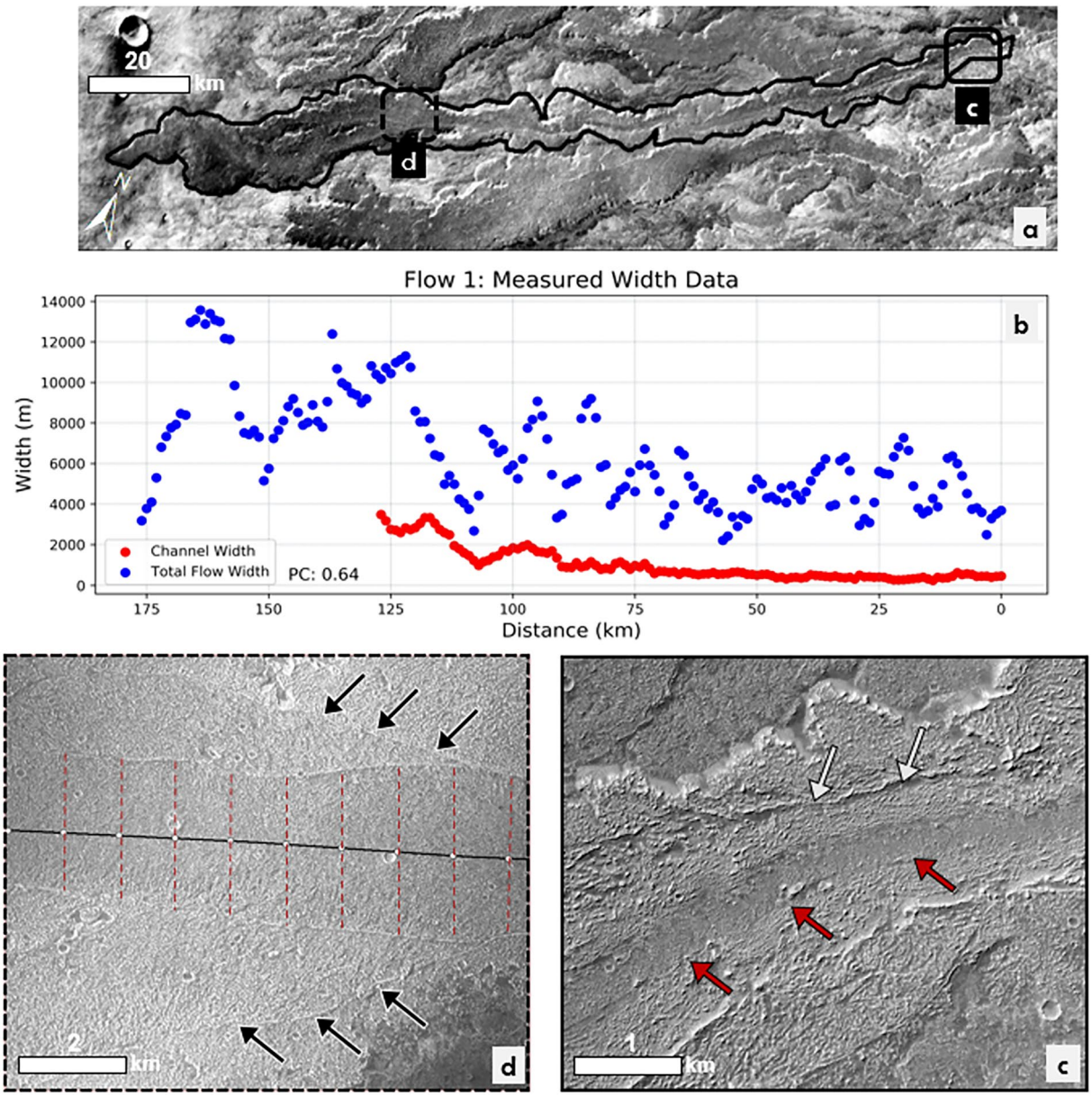

Figure 4. (a) THEMIS daytime TIR mosaic showing Flow 1 outlined in black. The black boxes indicate the regions shown in (c and d). (b) Plot of the central channel and total flow width measurements made using context camera (CTX) data. (c) CTX image (G15_024125_1596) of the black box in (a). The red arrows indicate the central channel, whereas the white arrows indicate an older central channel levee. (d) CTX image (P11_005177_1606) of the red dashed box in (a). The black line with white dots indicate the central channel and the black arrows show the locations on either side of the central channel where branching occurred.

Flow 4 (*long*): The upper two-thirds of the exposed 152 km flow have a fairly uniform width, whereas the lower third widens prominently and has large scale sinuosity. Flow texture is knobby but less rugged than Flow 1 (Figure 7). The channel, measured at 127 km, is sinuous and noticeably variable in width (Figure 7b), and the channel surface is clearly smoother than the surrounding flow surface (Figure 7c). The channel has an average rate of widening downflow of 26.3 m/1,000 km and follows a similar exponential trend as Flows 1 and 3. The observable flow covers an area of 758 km^2. Along the channel's length small islands are evident. About a third of the way down there is a 10 km segment of the central channel that is poorly defined on the northern side. This may be due to interaction with the adjacent flow. Along this section the channel becomes less sinuous, contains

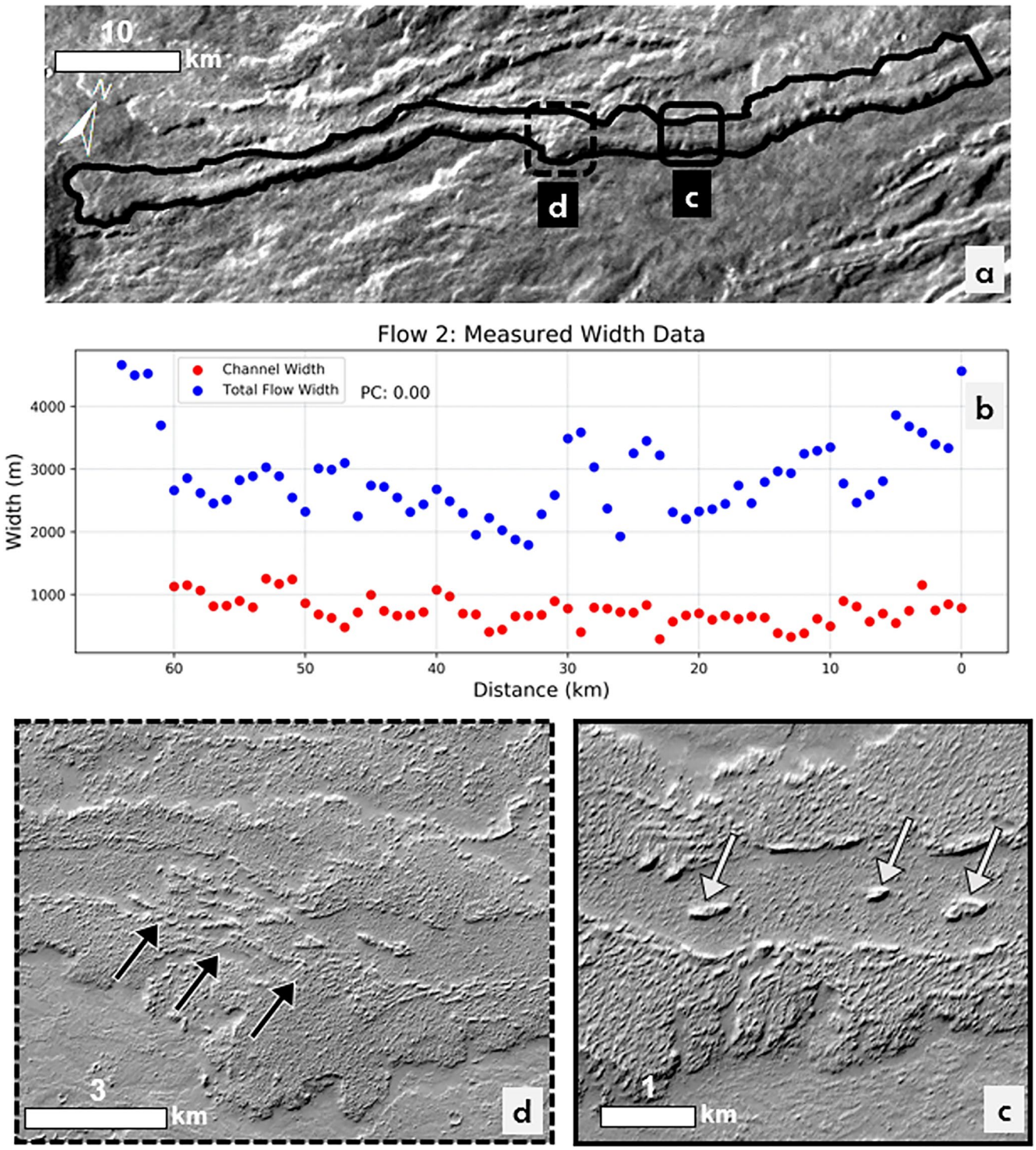

Figure 5. (a) THEMIS daytime TIR mosaic showing Flow 2 outlined in black. The black boxes indicate the regions shown in (c) and (d). (b) Plot of the central channel and total flow width measurements made using context camera (CTX) data. (c) CTX image (B20_017611_1624) of the black box in (a). The white arrows indicate three examples of islands that are present inside the central channel. (d) CTX image (B20_017611_1624) of the red dashed box in (a). The black arrows indicate a disruption in the levee and channel. One interpretation of this feature is a potential blockage that may have occurred during the emplacement of the flow and caused the wider levee to the south.

islands elongated in the flow direction, and the channel exhibits lower relief relative to the levee surface. Lineaments define the channel margins downflow and become more distinct (i.e., linear ridges) as the flow widens significantly in its distal segment (Figure 7d). Here the channel surface is knobby with irregular lineaments that suggest differential flow and crustal plates.

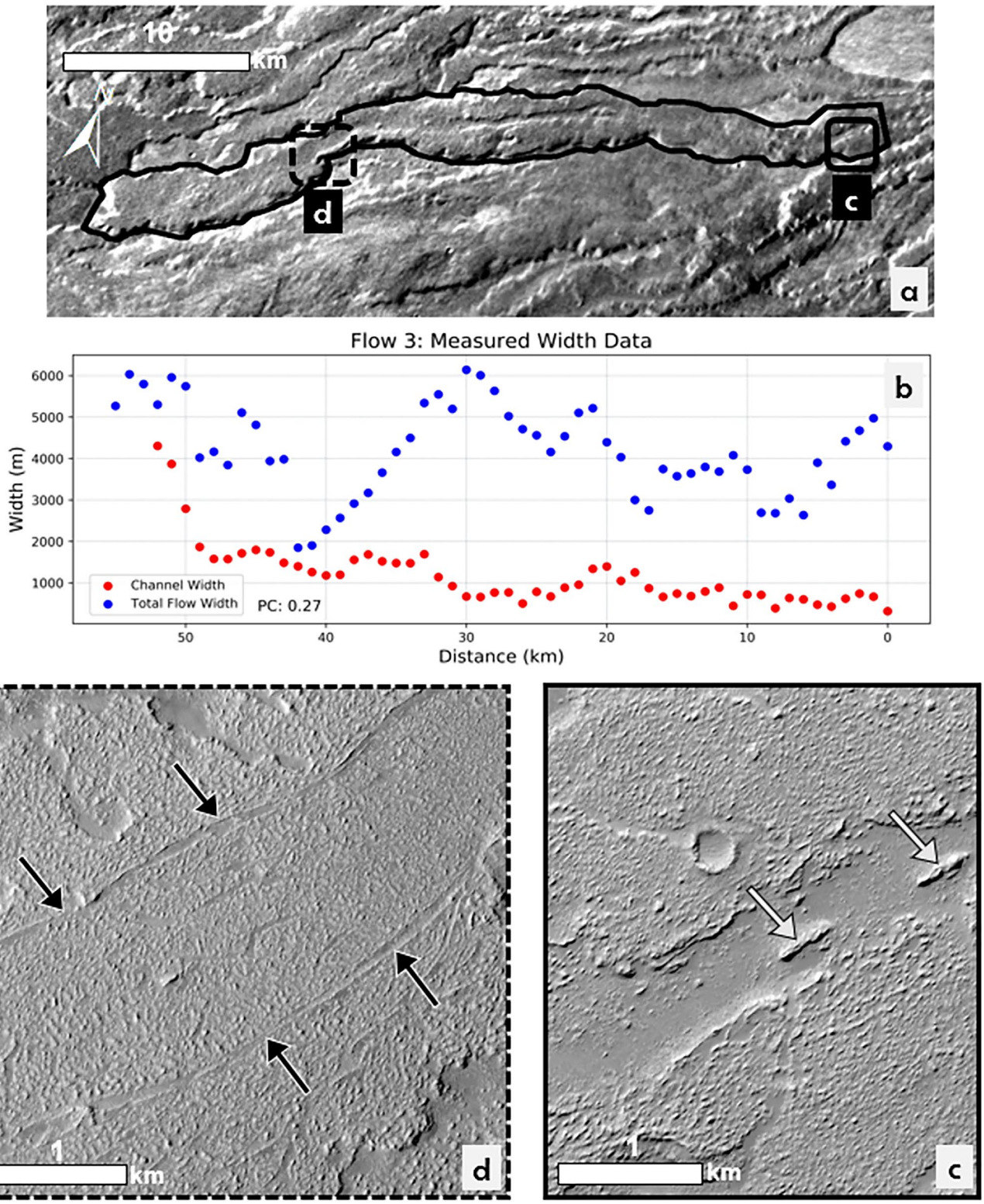

Figure 6. (a) THEMIS daytime TIR mosaic showing Flow 3 outlined in black. The black boxes indicate the regions shown in (c) and (d). (b) Plot of the central channel and total flow width measurements made using context camera (CTX) data. (c) CTX image (B20_017611_1624) of the black box in (a). The white arrows indicate two examples of islands that are present inside the central channel. The islands are elongated in the direction of the central channel. (d) CTX image (P06_003555_1604) of the red dashed box in (a). The black arrows show lower relief levees closer to the distal portion of the flow. This is different than the higher relief channels seen in (c).

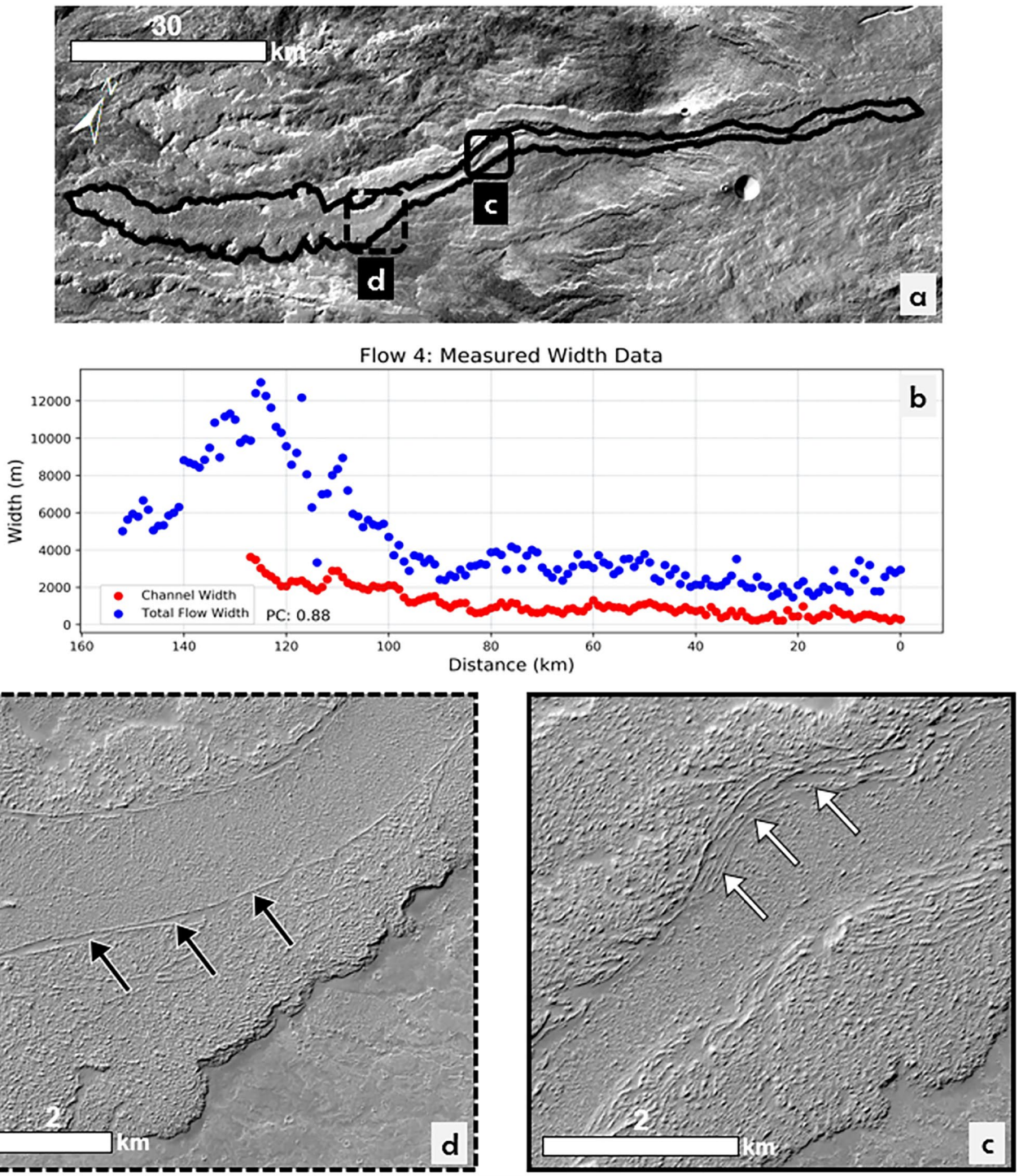

Figure 7. (a) THEMIS daytime TIR mosaic showing Flow 4 outlined in black. The black boxes indicate the regions shown in (c) and (d). (b) Plot of the central channel and total flow width measurements made using context camera (CTX) data. (c) CTX image (P02_001854_1636) of the black box in (a). The white arrows indicate stacked curve linear features along the central channel. These may indicate varying levels of the lava flow as it was emplaced. (d) CTX image (P02_001854_1636) of the red dashed box in (a). The black arrows show lower relief levees closer to the distal portion of the flow. This is similar to the features observed with Flow 3.

Flow 5 (*short*): The total flow length is 47 km with the central channel visible for 44 km (Figure 8). It is morphologically similar to Flows 2 and 3 but covers the smallest area at 152 km^2. The up-flow channel is more sinuous and less well-defined than downflow, where it is more linear to curvilinear. Numerous islands are present along the central channel (Figure 8c). Flow 5 is similar to Flow 2 in regards to the similar rate and trend of channel

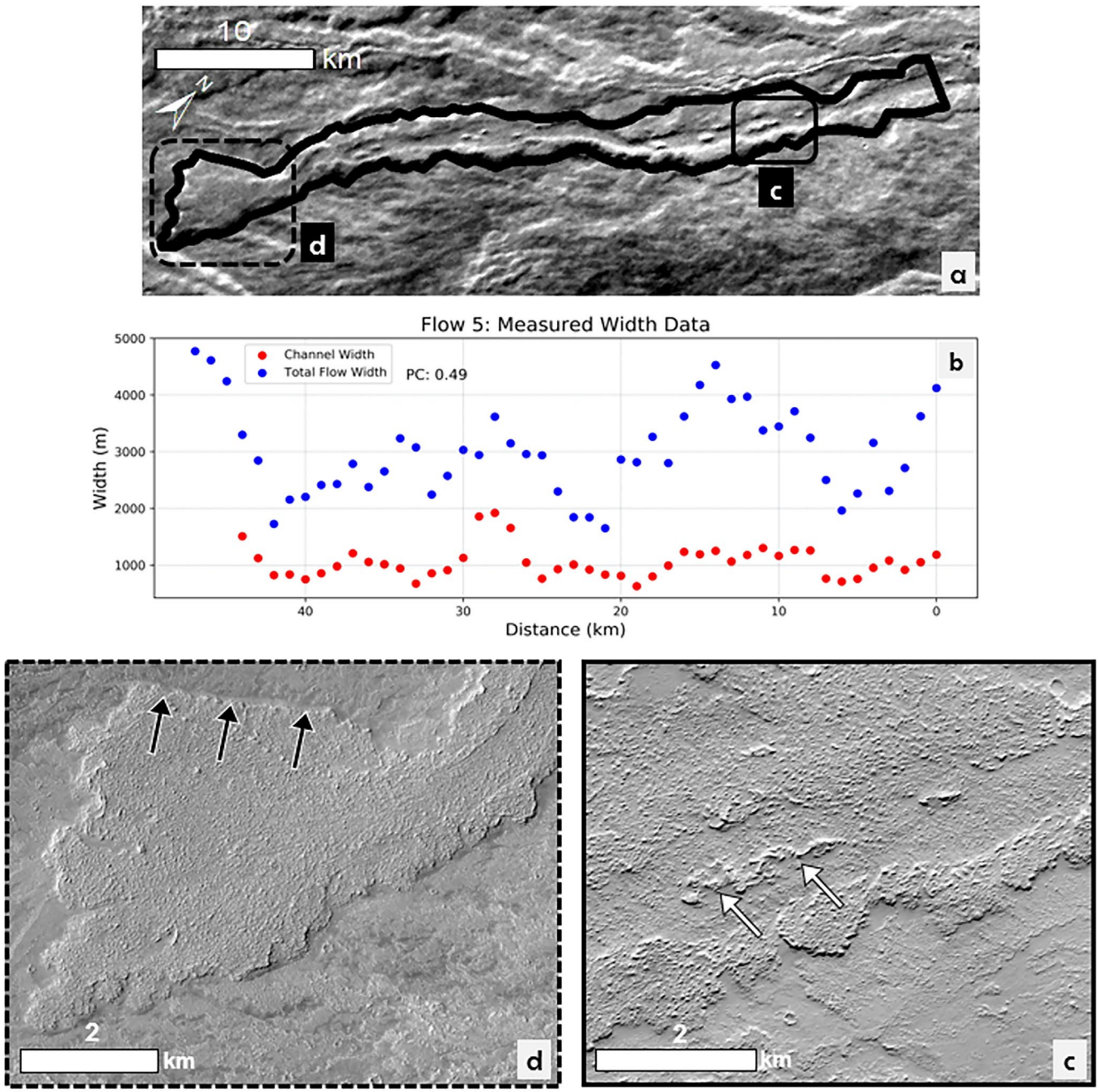

Figure 8. (a) THEMIS daytime TIR mosaic showing Flow 5 outlined in black. The black boxes indicate the regions shown in (c) and (d). (b) Plot of the central channel and total flow width measurements made using context camera (CTX) data. (c) CTX image (B20_017400_1634) of the black box in (a). The white arrows show a large island in the central channel. (d) CTX image (G10_022147_1632) of the red dashed box in (a). The black arrows indicate the distinct linear boundary at the distal flow front which is unusual in comparison to the other flows.

widening of 7.4 m/1000 m. Toward the flow terminus the channel widens and has distinct linear boundaries, which consists of a broad, spreading lobe with some parallel ridges at the front (Figure 8d). The surface texture of the channel and flow terminus suggest differential flow and crustal plates.

3.2. PyFLOWGO Results

During the application of PyFLOWGO, each of the model runs stopped due to the core reaching a solidus temperature of 1253 K (based on the Tolbachik analog flow), as opposed to the other stopping criteria: (a) the

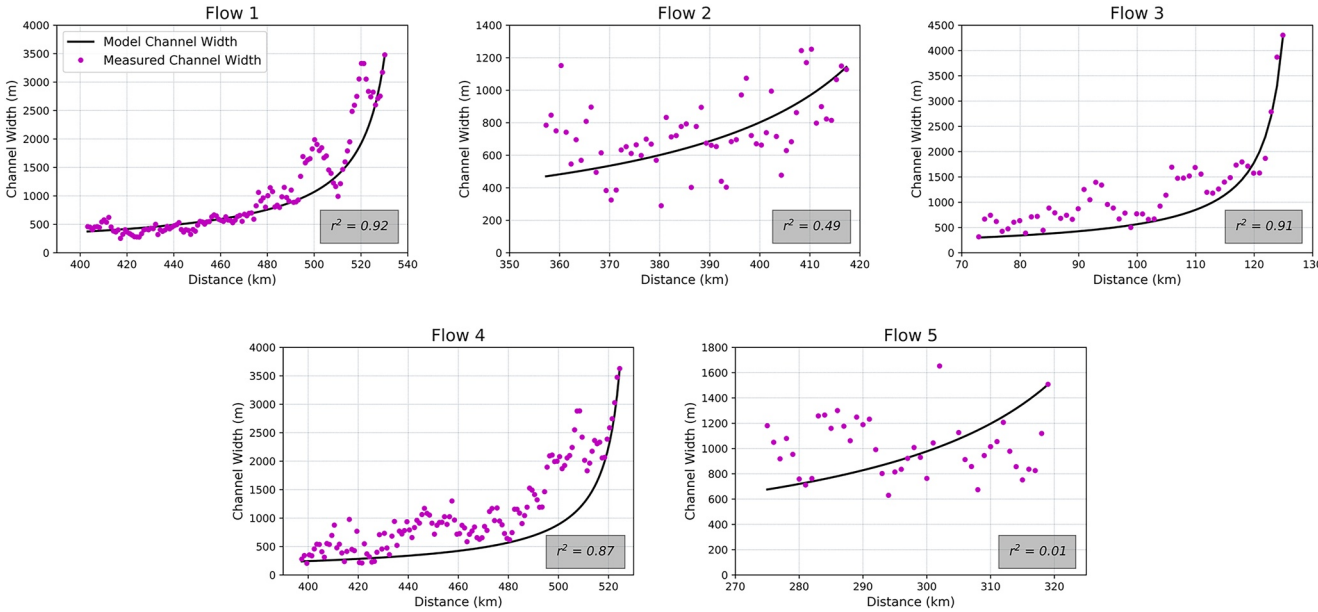

Figure 9. Plots of the modeled and measured central channel width versus the channel length. Flows 1, 3, and 4 show a statistically significant fit (r^2 values of 0.92, 0.91, and 0.87, respectively). Flows 2 and 5 do not (r^2 values of 0.49 and 0.01, respectively).

velocity reaching zero or (b) the yield strength of the flow core increases to a point where advance is impossible. For this step, each modeled channel length matched the measured channel lengths to <5%. For step 2, each final channel width matched the measured channel width to <5%. To further determine how well the model replicated other aspects of the flow's emplacement, the measured channel widths were compared to the modeled channel widths along the visible portion of each flow using a correlation coefficient. Channel width is allowed to vary in PyFLOWGO as a function of the velocity and the constant channel depth constraint. There is a notable decrease between the modeled starting channel width where compared to the observed starting channel width (Table 3). Flows 1, 3, and 4 showed a good fit between the measured and modeled channel widths (r^2 values of 0.92, 0.91 and 0.87, respectively) (Figure 9). However, Flows 2 and 5 did not show a statistically significant match (r^2 values of 0.49 and 0.01, respectively) (Figure 9). In addition to modeled channel length and channel width, PyFLOWGO also calculates the heat loss, core temperature, crystallization rate, crystal content, viscosity, yield strength, and flow velocity. Important to this study is to determine the actual channel lengths in order to locate vent source area(s) and also to assess whether prior modeling studies, relying only on the visible portions of the flows, produced accurate results. In addition, the PyFLOWGO modeling needed to determine the total channel lengths also produces the effusion rate, viscosity, and yield strength for each flow, which can be compared to past studies.

3.2.1. Effusion Rates

The average modeled effusion rate for the five flows was 4,960 $m^3\ s^{-1}$, ranging from 2,500 to 6,750 $m^3\ s^{-1}$ (Table 4). These values are an order of magnitude higher than recent terrestrial eruptions, including the 2012–2013 Tolbachik eruption (~247–440 $m^3\ s^{-1}$) and the 2018 Kilauea eruption (without pulses, ~400–500 $m^3\ s^{-1}$) (Dvigalo et al., 2013; Kubanek et al., 2017; Patrick et al., 2019).

In general, the five flows investigated are at the lower end of calculated values by Warner and Gregg (2003) for Arsia Mons (5,600–43,000 $m^3\ s^{-1}$) and at the upper range of those for Elysium Mons by Pasckert et al. (2012) (99–4,452 $m^3\ s^{-1}$). The Warner and Gregg (2003) study focused on large sheet-like flows, which likely accounts for their higher modeled effusion rates. Pasckert et al. (2012) investigated flow morphologies similar to this study. Both Warner and Gregg (2003) and Pasckert et al. (2012) utilized the Graetz method for determining effusion rate, which is different from our study. Finally, Flow 4 of our study was also one of the flows studied by Glaze et al. (2009), in which they modeled a much lower effusion rate of 25 $m^3\ s^{-1}$ (compared to 3,900 $m^3\ s^{-1}$ here). Glaze et al. (2009) used a hybrid model that accounts for the creation of levees during a

Table 4
Best-Fit Model Run Results for Effusion Rate, Viscosity, and Yield Strength for the Five PyFLOWGO Flows Modeled

	Effusion rate ($m^3\ s^{-1}$)	Average viscosity (Pa s)	Median viscosity (Pa s)	Minimum viscosity (Pa s)	Maximum viscosity (Pa s)	Maximum yield stength (Pa)
Flow 1	$5.40 \times 10^3 \pm 300$	7.27×10^4	4.25×10^4	2.31×10^4	6.70×10^5	381
Flow 2	$6.25 \times 10^3 \pm 250$	7.07×10^4	5.05×10^4	2.81×10^4	2.85×10^5	124
Flow 3	$2.50 \times 10^3 \pm 150$	3.18×10^4	1.79×10^4	9.47×10^3	2.84×10^5	124
Flow 4	$3.90 \times 10^3 \pm 150$	4.49×10^4	2.33×10^4	1.21×10^4	6.15×10^5	352
Flow 5	$6.75 \times 10^3 \pm 200$	5.66×10^4	4.11×10^4	2.31×10^4	2.14×10^5	66

Note. Morphometric variables used in these modeling results are the depth of the channel where is it first identified and the modeled channel width at the inferred vent location.

flow's progression. This hybrid model can best be described as a volume-limited model, whereas PyFLOWGO is cooling-limited.

3.2.2. Viscosity

To determine melt viscosity, we used one of the PyFLOWGO internal viscosity modules (Giordano et al., 2008) for the interstitial melt viscosity in association with the Einstein-Roscoe module for computing the effect of crystals (Table 1). The Einstein-Roscoe module is one of eight options available in PyFLOWGO, and was used for the terrestrial analog study of Ramsey et al. (2019). The average viscosity for the five flows was determined to be 5.5×10^4 Pa s. Values ranged from 9.4×10^3 to 6.6×10^5 Pa s (Table 4). The model also describes the change in viscosity over the length of the channel. The viscosity values are within the range determined for large terrestrial eruptions such as the 2012–2013 Tolbachik and the 2018 Kilauea eruptions (Belousov & Belousova, 2017; Soldati et al., 2021).

We use the PyFLOWGO modeled viscosity at the point of flow cessation to compare to other models/studies. The five flows are in the range of calculated values found by Warner and Gregg (2003) for Arsia Mons (10^4–10^7 Pa s) and similar to those determined by Vaucher et al. (2009) for flows in the Central Elysium Planitia (CEP) (6.9×10^2 to 2.5×10^5 Pa s). Our modeled values are slightly below the average found at Ascraeus Mons by Hiesinger et al. (2007) (4.1×10^6 Pa s). Finally, Flow 4 had a lower calculated final viscosity (6.1×10^5 Pa s) than the value (1.0×10^6 Pa s) reported in Glaze et al. (2009).

3.2.3. Yield Strength

PyFLOWGO also calculates yield strength as a function of lava temperature and crystallinity (Ryerson et al., 1988). See Chevrel et al. (2018) for specific details on the equations used. PyFLOWGO calculates the change in yield strength at each step until the flow stops. We then report the yield strength at the end of the flow, for direct comparison to other studies that calculate yield strength after the flow has been emplaced (e.g., Hiesinger et al., 2007; Peters et al., 2021; Vaucher et al., 2009). The average yield strength for the five flows was 209 Pa and ranged from 66 to 381 Pa (Table 4). Yield strengths determined for Flows 1 to 4 are similar to those measured for channelized basaltic flows at Mt. Etna (280–590 Pa) (Sparks et al., 1976) and slightly lower than those of the Holuhraun 2014–2015 basaltic eruption (316–2,511 Pa) (Kolzenburg et al., 2018). Our results are also similar to those found for the leveed flows in the CEP by Vaucher et al. (2009) (5–173 Pa). However, they are noticeably lower than those calculated by Hiesinger et al. (2007) at Ascraeus Mons (677–4.91×10^4 Pa) and channelized flows in Peters et al. (2021) using the self-replication lava flow model (1.4×10^3 to 3.6×10^4 Pa), both of which are much higher than typical basaltic flows.

3.3. Finding Potential Vent Locations

Following determination of the total modeled channel lengths, the five flows all project upslope to locations close to the base of Arsia Mons on the southern flow apron. Projected starting points for Flows 1, 3, and 5

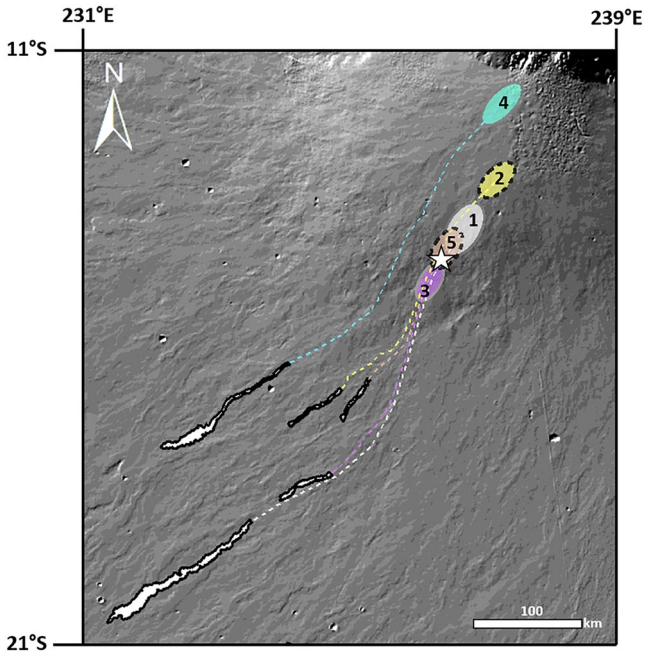

Figure 10. The five flows of the study with the back projected tracks shown by dashed lines. Back projection is done by using a 2° slope and following the regional aspect and slope vectors. Colored ellipse represent the error range associated with the context camera (CTX) and MOLA measurements. The dashed line around the ellipse for Flows 2 and 5 indicate the increased uncertainty in those results based on our initial modeling (in this figure). Flows 1, 3 and 5 (and possibly 2) cluster together in the same region, whereas Flow 4 projects back to a different area. White star shows the location of the possible vent source (Figure 11). Base image is MOLA/HRSC blended DEM hillshade.

cluster together in the same general area, with Flow 2 slightly further upslope and Flow 4 projecting to a different area closer to the base of Arsia Mons (Figure 10). An error ellipse is shown around each of the possible flow initiation points that is based on the uncertainties in the CTX and MOLA data. Specifically, these ellipse areas represent the propagation in the modeling of the errors in measuring the starting channel width (±6 m) and depth (±1 m). However, Flow 2 and had a much poorer statistical fit between the measured and modeled channel width from Step 2 (Figure 9). This is likely due to effusion rate variations/pulses or channel blockages, each of which would cause variations in flow velocity resulting in changes to the channel width that are beyond the scope of PyFLOWGO. This then would result in a higher uncertainty in the modeled effusion rate, which is calculated from the first application of PyFLOWGO. Modeling the total channel length in the second application of PyFLOWGO uses the effusion rate plus the dimensions of the channel where it first is visible to initiate the narrowing upslope assumption. Therefore, although the results shown in Figure 9 do not have a direct bearing on estimating the total channel length and possible vent locations, they do add further uncertainty. For example, a slightly lower effusion rate would result in a shorter overall flow length that would cause the Flow 2 error ellipse to shift downslope closer to those of Flows 1, 3, and 5. It is possible, therefore that all of the flows except for Flow 4 originate from the same location. This is corroborated by examining the patterns of other flows seen in the CTX data. Their surface morphology suggests that Flows 1 to 3 and 5 emanate from the same area and extend to the south, developing into multiple larger, distinctive flows downslope (Figure 11c).

Investigation of the area within the ellipses for these four flows identified a possible source (Figure 11a). The feature is a long (~48 km) sinuous rille with a measured average width of ~873 m using the CTX data. The inner walls of the rille show layering in the upper sections, suggesting that it could be composed of consolidated material, likely overlaping lava flows (Figure 11b). The layering characteristics observed are similar to linear vents to the east of Arsia Mons identified by Hauber et al. (2009). Visual investigation of the shadows cast into the rille indicates that it is deeper and wider at its northern extent and gradually becomes shallower and narrows to the south. The depth of the feature at its southern terminus (~207 m) was determined from three MOLA PEDR transects. Its location relative to the volcano's summit is consistent with terrestrial rift-analogs such as Hawai'i, the Galapagos, and Tolbachik, where large volume, channelized flows commonly originate from rift-aligned vents on the lower flanks rather than at the summit caldera (Rowland et al., 2002). This process was observed in the 2018 Kilauea eruption where multiple channelized flows originate from the same vent over the course of an eruption (Mouginis-Mark et al., 2022). Flank aligned vents have also been observed at Ascraeus and Pavonis Montes (Bleacher et al., 2007).

Investigation of the back-projected region for Flow 4 using both CTX and MOLA did not reveal any obvious vent structures; however, this does not preclude the presence of vents in this region, which has a moderately-high dust-cover index derived from IR data. That observation indicates thicker dust mantling that could obscure a potential vent (Ruff & Christensen, 2002). Younger lava flows, pyroclastic deposits, or tephra fallout could also have covered any vents in the error ellipse region of Flow 4.

4. Discussion

The PyFLOWGO based modeling results of effusion rate, viscosity, and yield strength fall within the ranges of prior studies of Arsia Mons and other volcanic regions, which helps to validate the model's applicability to Mars (Table 5). However, PyFLOWGO, as with any lava flow emplacement model, is not capable of accounting for

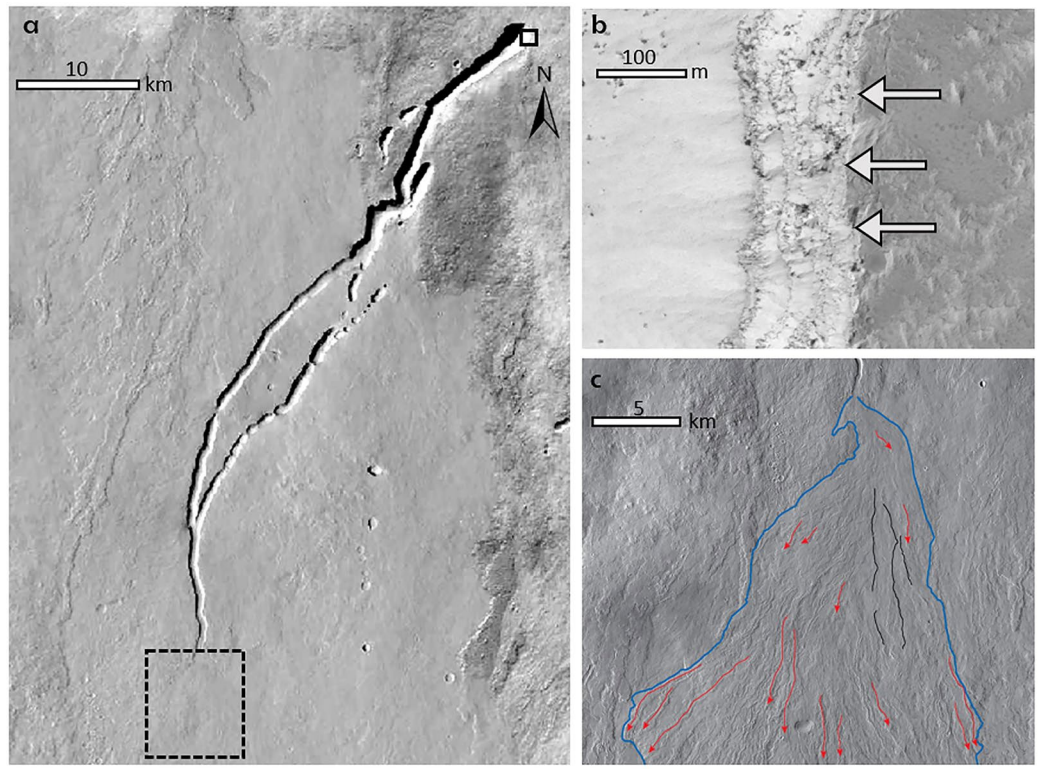

Figure 11. (a) Context camera (CTX) mosaic showing the potential source/vent for Flows 1, 3, and 5 (and possibly Flow 2) (feature is centered at 14.5°S, 237.5°E). The black solid and dashed line boxes indicate the regions shown in (b) and (c), respectively. (b) The layering along the rille wall (indicated by white arrows) is similar to that seen in linear vents identified east of Arsia Mons (Hauber et al., 2009). Base image for (b) is from the HiRISE instrument (ESP_068341_1655). (c) Lava fan emanating from the end of the rille structure (shown by the blue line), which develops into a full flow field further south. The black lines indicate lava channels, and the red arrows denote lava flows.

Table 5
Compilation of Effusion Rate, Viscosity, and Yield Strength Calculations From Literature

Source	Volcano	Effusion rate range (m^3/s)	Viscosity (Pa s)	Yield strength (Pa)
Hulme (1976)	Olympus Mons	380 to 470	2.3×10^5 to 6.9×10^6	8.8×10^3 to 4.5×10^4
Zimbelman (1985)	Ascraeus Mons	18 to 60	6.5×10^5 to 2.1×10^8	3.3×10^3 to 8.3×10^4
Cattermole (1987)	Alba Patera	155 to 5.8×10^3	1.3×10^5 to 1.9×10^6	1.9×10^3 to 2.8×10^4
Lopes and Kilburn (1990)	Alba Patera	700 to 1×10^5	NA	NA
Wilson and Mouginis-Mark (2001)	Elysium Mons	3.4×10^3 to 1.3×10^4	NA	NA
Warner and Gregg (2003)	Arsia Mons	5.6×10^3 to 4.3×10^4	1.6×10^4 to 1.6×10^8	2.5×10^3 to 3.9×10^3
Basilevskaya and Neukum (2006)	Olympus Mons	24 to 137	1.4×10^3 to 2.8×10^7	900 to 3.6×10^4
Hiesinger et al. (2007)	Ascraeus Mons	23 to 404	1.8×10^4 to 4.2×10^7	677 to 4.9×10^4
Glaze et al. (2009)	Tharsis	25 to 840	3.0×10^5 to 3.6×10^6	NA
Vaucher et al. (2009)	Central Elysium Planitia	19 to 8×10^4	2 to 2.5×10^5	100 to 500
Pasckert et al. (2012)	Elysium Mons	99 to 4.4×10^3	1.2×10^5 to 3.1×10^7	380 to 1.5×10^4
Peters et al. (2021)	Tharsis	0.3 to 3.5×10^4	9.4×10^4 to 7.4×10^7	800 to 3.6×10^4

Note. Values for each of these studies were calculated through a variety of methods, including flow measurements, terrestrial values for basaltic lava flows (density, yield strength), Graetz number, Jeffrey's equation, and/or individually designed models.

all relevant processes. Discrepancies in results relative to those in the literature can be attributed to the different methods used to determine the emplacement and rheologic parameters, and the varied flow morphologies investigated. In its standard approach, PyFLOWGO enables the capability to model the rheological properties of the visible portions of lava flows by fitting their channel lengths. Here, we have expanded beyond prior terrestrial PyFLOWGO modeling efforts to examine the same flow from two different perspectives (modeling both channel length and width). The first application to the visible portion of the flow relies on the assumption of constant channel depth to fit the exposed channel length and derive an effusion rate (as well as rheologic parameters). The second application, uses that effusion rate and fitting of the exposed channel width to estimate the total channel length, and thus approximate a vent location upslope. During this second application of modeling the total channel length, rheological properties are also determined. These results represent the total channel extent rather than just the exposed portion.

The modeled channel lengths range from 124 to 530 km (Table 3). These lengths are ∼4 times longer than the observed/measured lengths of the exposed parts of the channels. Channelized flows of these lengths would suggest long lived eruptions and sustained subsurface magmatic pathways. Although the modeled lengths are longer than typically observed for channelized flows around Arsia Mons (presumably due to burial), lengths of this magnitude are observed in other regions on Mars, including channelized flows associated with Ascraeus Mons flows (Garry et al., 2007) and the leveed channel system that supplies the flow field southwest of Tyrrhenus Mons (Crown et al., 2020).

4.1. Interpreting Model Results

As highlighted by Warner and Gregg (2003), interpreting planetary rheological modeling results requires caution. PyFLOWGO is no exception and we highlight a few points that should be considered before interpreting the effusion rate, viscosity, and yield strength results.

A steady or constant effusion rate is not common over the entire course of any terrestrial eruption, though it can be for significant portions. There is no reason to believe this should be different on Mars. Almost all eruptions have variable effusion rates with a general decrease over time (Bonny et al., 2018; Harris et al., 2000). PyFLOWGO only uses a single effusion rate for a model run, best described as an *effective* effusion rate. As defined by Rowland et al. (2005), an effective effusion rate is used to reproduce the maximum channel length that a cooling-limited flow can reach and is roughly half the maximum effusion rate (Rowland et al., 2005). Following this relationship, the maximum effusion rate for the five flows investigated here would be ∼13,500 $m^3\ s^{-1}$. However, the relationship between effective and maximum effusion rate is not well constrained.

Comparing results from Steps 1 and Step 2 upon flow cessation shows that there is not a significant difference in modeled final values of flow viscosity (Figure 12a) (Table 6). However, there are significant differences in the downflow rate of change in rheologic parameters and how well the modeled channel width matches the measured channel width. Using Flow 1 as an example, the average rates of change of viscosity are 5.0 and 1.2 Pa s per m for Steps 1 and 2, respectively. The rate of viscosity change produced in Step 2 of the modeling is more similar to what has been observed for terrestrial basaltic lava flows of 2.6 Pa s per m (e.g., Harris et al., 2007); whereas, the rate of viscosity change in Step 1 is nearly double to that observed for terrestrial basaltic flows. There is also a much improved correlation between the measured channel widths and modeled channel widths in Step 2 (Figures 12b and 12c). The modeled channel widths from Step 2 closely match the measured channel widths.

Comparison of the Step 2 modeled viscosity and yield strength results to those in the literature shows that our values are at the low end of the range of previous estimates (Table 5). Two of the input parameters that were used from the Tolbachik analog during the first PyFLOWGO application were the starting crystal fraction and crystals grown during cooling. The crystallinity of the lava flow has a direct impact on both the viscosity and yield strength (see equations in Chevrel et al. (2018)). Comparing the values from Tolbachik for starting crystal fraction and crystals grown during cooling to other lava flows modeled using PyFLOWGO (i.e., Mauna Loa 1984, Mauna Ulu 1974, and Piton de la Fournaise 2010) we found the starting crystal fraction to fall within a normal range, but the percent of crystals grown during cooling to be lower. For Tolbachik the percent of crystals grown during cooling is 37% whereas for the other three studies it ranged from 45% to 89% (Chevrel et al., 2018; Ramsey et al., 2019). Increasing the starting crystal fraction and/or crystals grown during cooling of the modeled

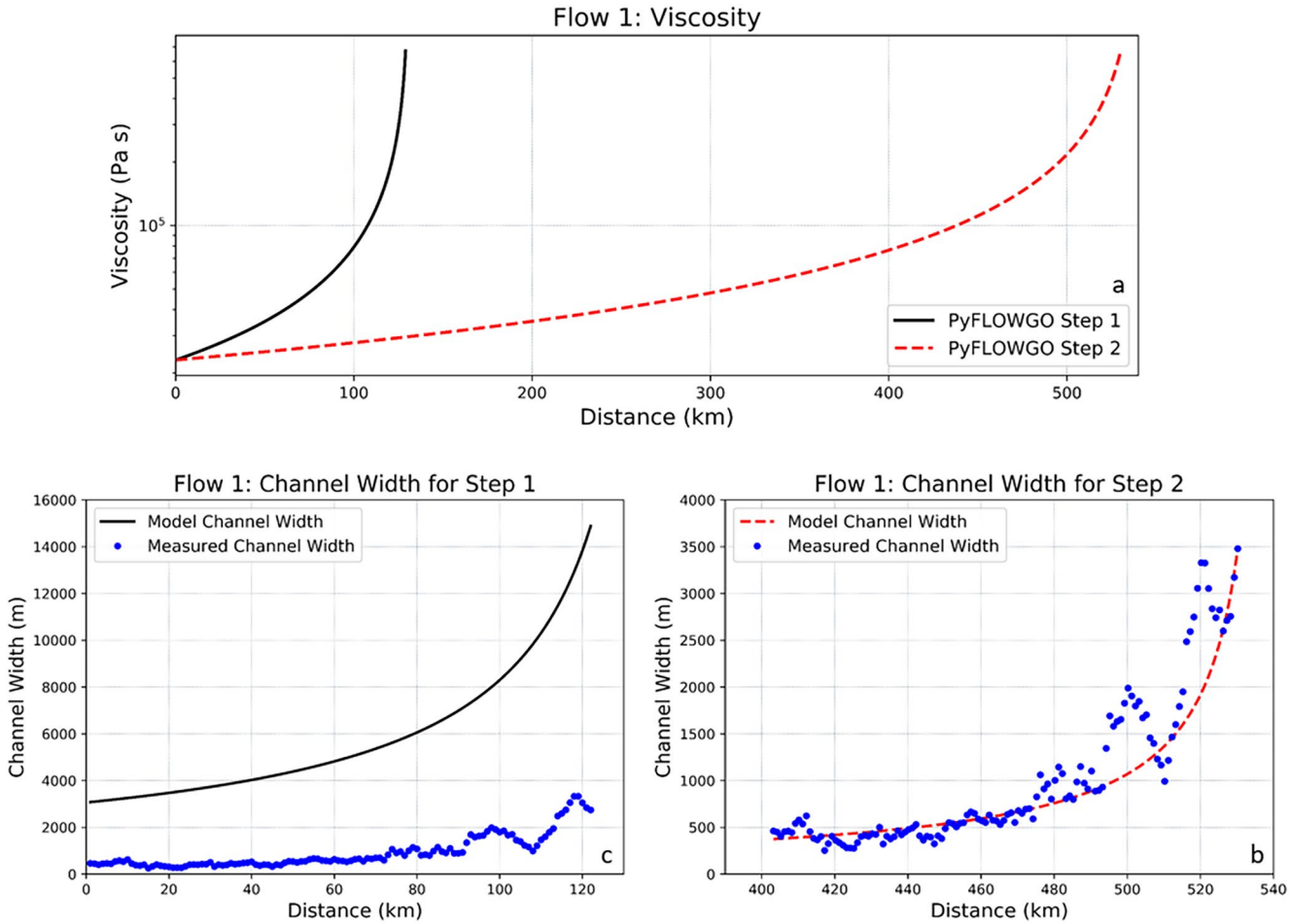

Figure 12. (a) The difference in viscosity for Flow 1 between Step 1 and Step 2 of the PyFLOWGO modeling method. (b and c) compare the model channel width and the measured channel width for Step 1 and Step 2, respectively.

lava flow will directly increase the yield strength and viscosity, and by extension decrease flow length and velocity (Wantim et al., 2013).

Table 6
Comparison of the Model Results for Viscosity From PyFLOWGO for Steps 1 and 2 for the Five Flows Modeled

	Model step	Starting viscosity (Pa s)	Final viscosity (Pa s)	Rate of change (Pa s per m)
Flow 1	Step 1	2.31×10^4	6.71×10^5	5.03
	Step 2	2.31×10^4	6.71×10^5	1.22
Flow 2	Step 1	2.81×10^4	2.85×10^5	4.29
	Step 2	2.81×10^4	2.85×10^5	0.62
Flow 3	Step 1	9.47×10^3	2.84×10^5	5.16
	Step 2	9.47×10^3	2.84×10^5	2.19
Flow 4	Step 1	1.21×10^4	6.58×10^5	5.06
	Step 2	1.21×10^4	6.15×10^5	1.15
Flow 5	Step 1	2.31×10^4	2.14×10^5	4.36
	Step 2	2.31×10^4	2.14×10^5	0.59

The terrestrial analog used for this study (Tolbachik 2012–2013 eruption) emplaced basaltic trachyandesite lava. Historically, a Hawaiian basalt has been used as a Martian analog (Mouginis-Mark et al., 2022). We acknowledge that using a basalt or a basaltic andesite as an analog may have an impact on the rheologic modeling results. However, as described previously, Tolbachik had numerous reasons that made it the preferred analog for this study. Furthermore, the modeled viscosity values fell at the lower end of the ranges from prior studies; therefore, the use of a basaltic trachyandesite lava analog did not produce more viscous flows.

4.2. Comparison to Previous Modeling Studies

Flow 4 is one of the six flows (their Flow 6) investigated by Glaze et al. (2009) using a hybrid model. The hybrid model combines two models of levee formation (construction during passage of the flow front and growth along the entire length of the flow) and detailed flow measurements in order to estimate volumetric flow rate, eruption duration, and viscosity (Glaze et al., 2009). For this same flow, we determined an effusion rate of 3,900 $m^3\ s^{-1}$ and a maximum

viscosity of 6.15×10^5 Pa s, compared to 25 $m^3 s^{-1}$ and 1.0×10^6 Pa s, respectively by Glaze et al. (2009). Their hybrid model uses detailed flow measurements (flow length, central channel width, levee width, flow thickness), but only assumes heat loss through the conductive cooling law used by Hon et al. (1994). PyFLOWGO accounts for all heat losses and gains under Martian conditions.

The effusion rates determined by Glaze et al. (2009) are one to two orders of magnitude lower than previous calculations for Martian lava flows (Table 5). Given the observed size of the central channel (average width of 1,129 m) and modeled channel lengths (524 km) for Flow 4, larger effusion rates are likely required to produce and maintain these channel dimensions. Sustaining a lower effusion rate over a longer period of time would promote cooling and inhibit creation of the large-scale morphological features, such as the consistent, large central channel and prominent levees (e.g., Kerr et al., 2006). Furthermore, effusion rates comparable to those of large terrestrial flows produce a smaller flow size on Mars due to the gravity and cooling (e.g., Rowland et al., 2004). It is likely that neither model result is 100% accurate due to assumptions that fail to adequately represent different complexities of the flow emplacement process. However, the results produced by PyFLOWGO corroborate the observed flow morphological features and are consistent with other prior studies. However, the primary advantage of using PyFLOWGO here is that we are able to also produce the entire channel length for each flow and therefore, identify potential vent source regions, which is not possible with any prior modeling study.

4.3. Model Limitations: Topography

Our modeling assumed a constant slope of 2°. This assumption is consistent with previous Martian applications of PyFLOWGO (e.g., Rowland et al., 2002, 2004) and with other modeling studies of Martian flows where the pre-flow topography is not known (e.g., Baloga & Glaze, 2008; Garry et al., 2007). Typically, terrestrial applications of PyFLOWGO use a known pre-flow topographic profile derived from a high-resolution DEM (Harris et al., 2016; Harris & Rowland, 2001). Other studies have shown that certain models are sensitive to the DEM used and that a constant slope is not always appropriate for modeling planetary lava flows (Bilotta et al., 2019; Flynn et al., 2021; Glaze & Baloga, 2007). To assess the assumption of a constant 2° slope, we extracted a DEM profile adjacent to each flow from the MOLA/HRSC DEM. Each transect was devoid of interference from the flow levees but due to the complicated nature of the flow field, it is unlikely to represent the true pre-existing topography. The median slopes over the lengths of all five flows were less than 0.5° (Table 3). However, further upslope over the region used for the back projections, the slope is closer to 2° and therefore each of the flows were likely emplaced over topography between 0.5° and 2°. This is corroborated by the PyFLOWGO model results where the measured and modeled channel widths of Flows 1, 3, and 4 match well (Figure 9). This correlation is due either to the pre-flow topography being steeper and/or having a constant slope; and/or the resolution of the MOLA/HRSC DEM, which smooths the topography to an extent thus muting smaller scale topographic changes that could impact the flow's emplacement. The effect of low resolution DEMs underestimating topography and thus slope has been observed on Earth (Kienzle, 2004) but has not been sufficiently studied on Mars.

The use of a constant slope may not be suitable in the modeling of all flows on Mars, particularly for flows that may have a complex emplacement history (e.g., Flows 2 and 5). Our back-projection modeling of these five flows shows that 52%–86% of the channel lengths are buried up-slope by younger flows, meaning that their initial emplacement could have been over more variable and steeper topography. Given the model results, the complex nature of the Arsia Mons flow field, and the lack of pre-flow topography, the use of a constant slope that is an average between the upper flanks of Arsia Mons and the lower plains of Daedalia Planum was assumed appropriate.

4.4. Model Limitations: Emplacement Processes

As mentioned, the comparison between the measured and modeled channel widths for Flows 2 and 5 did not show a significant correlation. A more detailed investigation of each of these flows revealed possible examples of emplacement processes that are beyond the ability of PyFLOWGO to reproduce. At ~53 km for Flow 2 and ~26 km for Flow 5, there is evidence that the central channel was blocked for an unknown period during

the flow emplacement (Figure 6d). This is shown by the sudden widening of the flow width, combined with a sudden change in flow texture, from a knobby central channel to large knobs and ridges along the central channel (Figure 6d). A blockage or lava flow dam would impact the continuous growth and formation of the central channel. Replicating or accounting for roofing over, blockages, or lava flow dams is outside the capabilities of PyFLOWGO. However, the channelized flow length and final channel width were still reproduced. This indicates that the effusion rate and viscosity calculations for each of the flows were not significantly impacted. Combining lava flow modeling with analyses of flow morphology enables a more complete interpretation of PyFLOWGO's results.

5. Conclusions

Previous modeling studies of Martian lava flows have made use of fluid mechanics, wax analog experiments, numerical models, and detailed physical measurements. Studies of Martian lava flows are typically limited by burial of their proximal regions and commonly hindered by a lack of identifiable vents.

In this study, we applied a modified and well-constrained version of the PyFLOWGO model to five channelized flows southwest of Arsia Mons. With the flexibility of PyFLOWGO, we were able to first determine the effusion rates by modeling the exposed channel length. The effusion rates served as input to the second application of the model, using measured channel widths to estimate total channel lengths as well as calculate the lava viscosities and yield strengths. The accuracy of the model results was checked against image-based measurements of the channel lengths and widths for each application of PyFLOWGO. Our modeling determined that the lava flows in the southwest Arsia Mons flow fields were emplaced with effusion rates an order of magnitude higher than those common for larger, modern terrestrial eruptions. However, they had similar viscosities and yield strengths to the terrestrial flows of the same composition as well as the results from prior studies. The rheological results also place these flows into the basaltic compositional field.

The second application of PyFLOWGO attempted to match the final channel width to determine the full channel length (and with those values, possible vent/source locations) which is unique to this study. It is the first time that a model was used to estimate the total channel lengths of Martian lava flows that are not fully exposed in order to search for possible vent locations. Results reveal that these flows are on average four times longer than assumed based on mapping only the exposed portions. Model results show that four of the five flows investigated (Flows 1, 3, 5, and possibly 2) back-project to a likely vent location in a region of a known lava flow source. Although PyFLOWGO in general, this methodology specifically, has limitations the results are promising and can be corroborated with detailed morphologic studies, as was done here. Incorporating other plausible model inputs (i.e., using a different terrestrial analog or topographic profile) will increase the range in the model results. However, we believe the methods and results presented here are a strong foundation for future studies.

Due to the complicated nature of the flow field surface southwest of Arsia Mons and partial burial of older flows by younger flows, flows cannot commonly be traced to their source vents. Our modeling approach estimates the total channel lengths and potential source vent locations, suggesting flows southwest of Arsia Mons reach up to ~500 km in length. With the ability to connect more flows to potential vents, we can begin to compile a more complete record of the SW Arsia flow field evolution. Identification of potential vents could also be utilized to possibly determine subsurface magmatic pathways that have previously been unknown. This study has shown that PyFLOWGO is an effective model to reproduce the emplacement conditions of Martian channelized flows. Future applications of this approach include other flows in the Daedalia Planum, Elysium Mons, and other Tharsis volcanoes, as well other planetary environments (e.g., Venus and Io).

Data Availability Statement

All flow measurements and PyFLOWGO results discussed in this paper are available to the public (Flynn, 2022). The NASA datasets (CTX, HiRISE, THEMIS, and MOLA) used in this manuscript are publicly available through online archives and catalogues including NASA's Planetary Data System (pds.nasa.gov) and JMARS (jmars.asu.edu): (a) HiRISE (McEwen, 2007); (b) CTX (Malin, 2007); (c) THEMIS (Christensen, 2002); and MOLA (Smith et al., 2003).

Acknowledgments
This research was supported through NASA's SSW Program (80NSSC19K0547). The authors would like to thank Tracy Gregg, Sean Peters, and two anonymous reviewers for their helpful and constructive feedback on the manuscript. Thank you to Scott Rowland for his support to continue this work and Peter Mouginis-Mark for his helpful discussions.

References

Baloga, S. M., & Glaze, L. S. (2008). A self-replication model for long channelized lava flows on the Mars plains. *Journal of Geophysical Research: Planets*, *113*(5), 1–15. https://doi.org/10.1029/2007JE002954

Baloga, S. M., Mouginis-Mark, P. J., & Glaze, L. S. (2003). Rheology of a long lava flow at Pavonis Mons, Mars. *Journal of Geophysical Research: Planets*, *108*(7), 1–10. https://doi.org/10.1029/2002je001981

Basilevskaya, E. A., & Neukum, G. (2006). The Olympus volcano on Mars: Geometry and characteristics of lava flows. *Solar System Research*, *40*(5), 375–383. https://doi.org/10.1134/s0038094606050029

Beauchamp, N. (2017). Numerical modeling of the daedalia planum lava flows, Mars (MS Thesis). *University of Pittsburgh*. Retrieved from http://d-scholarship.pitt.edu/33602/

Belousov, A., & Belousova, M. (2017). Dynamics and viscosity of 'a'a and pahoehoe lava flows of the 2012–2013 eruption of Tolbachik volcano, Kamchatka (Russia). *Bulletin of Volcanology*, *80*(1), 6. https://doi.org/10.1007/s00445-017-1180-2

Berman, D. C., & Crown, D. A. (2019). Chronology of volcanism in southern tharsis, Mars: Constraints from lava flows in daedalia planum. In *46th Lunar and Planetary Science Conference*.

Bilotta, G., Cappello, A., Hérault, A., & del Negro, C. (2019). Influence of topographic data uncertainties and model resolution on the numerical simulation of lava flows. *Environmental Modelling & Software*, *112*, 1–15. https://doi.org/10.1016/j.envsoft.2018.11.001

Bleacher, J. E., Greeley, R., Williams, D. A., Cave, S. R., & Neukum, G. (2007). Trends in effusive style at the Tharsis Montes, Mars, and implications for the development of the Tharsis province. *Journal of Geophysical Research: Planets*, *112*(9), 1–15. https://doi.org/10.1029/2006JE002873

Bonny, E., Thordarson, T., Wright, R., Höskuldsson, A., & Jónsdóttir, I. (2018). The volume of lava erupted during the 2014 to 2015 eruption at Holuhraun, Iceland: A comparison between satellite- and ground-based measurements. *Journal of Geophysical Research: Solid Earth*, *123*(7), 5412–5426. https://doi.org/10.1029/2017JB015008

Carr, M. H., Greeley, R., Blasius, K. R., Guest, J. E., & Murray, J. B. (1977). Some Martian volcanic features as viewed from the Viking orbiters. *Journal of Geophysical Research*, *82*(28), 3985–4015. https://doi.org/10.1029/js082i028p03985

Cashman, K. V., Soule, S. A., Mackey, B. H., Deligne, N. I., Deardorff, N. D., & Dietterich, H. R. (2013). How lava flows: New insights from applications of lidar technologies to lava flow studies. *Geosphere*, *9*(6), 1664–1680. https://doi.org/10.1130/GES00706.1

Cattermole, P. (1987). Sequence, rheological properties, and effusion rates of volcanic flows at Alba Patera, Mars. *Journal of Geophysical Research*, *92*(6), 553–560. https://doi.org/10.1029/jb092ib04p0e553

Chevrel, M., Harris, A. J. L., & Rowland, S. K. (2018). PyFLOWGO: An open-source platform for simulation of channelized lava thermo-rheological properties. *Computers & Geosciences*, *111*, 167–180. https://doi.org/10.1016/j.cageo.2017.11.009

Christensen, P. R. (2002). 2001 Mars odyssey thermal emission imaging system infrared geometrically registered images.

Christensen, P. R., Jakosky, B. M., Kieffer, H. H., Malin, M. C., Mcsween, H. Y., Nealson, K., et al. (2004). The thermal emisson imaging system (THEMIS) for the Mars 2001 odyssey mission. *Space Science Reviews*, *110*(1/2), 85–130. https://doi.org/10.1023/b:spac.0000021008.16305.94

Chuang, F. C., Crown, D. A., & Tornabene, L. L. (2016). Zumba crater, Daedalia Planum, Mars: Geologic investigation of a young, rayed impact crater and its secondary field. *Icarus*, *269*, 75–90. https://doi.org/10.1016/j.icarus.2016.01.005

Crown, D. A., Berman, D. C., & Ramsey, M. S. (2015). Lava flow fields of Southern Tharsis, Mars: Flow types, interactions, and ages. In *46th Lunar and Planetary Science Conference*.

Crown, D. A., & Ramsey, M. S. (2017). Morphologic and thermophysical characteristics of lava flows southwest of Arsia Mons, Mars. *Journal of Volcanology and Geothermal Research*, *342*, 13–28. https://doi.org/10.1016/j.jvolgeores.2016.07.008

Crown, D. A., Ramsey, M. S., & Berman, D. C. (2012). Morphologic and chronologic studies of lava flow fields in the southern Tharsis region of Mars. In *43rd Lunar and Planetary Science Conference*.

Crown, D. A., Zimbelman, J. R., & Williams, D. A. (2020). The Circum-Hellas province. *The Volcanoes of Mars*, *93*.

Crumpler, L. S., & Aubele, J. C. (1978). Structural evolution of Arsia mons, Pavonis mons, and Ascreus mons: Tharsis region of Mars. *Icarus*, *34*(3), 496–511. https://doi.org/10.1016/0019-1035(78)90041-6

Dietterich, H. R., Cashman, K. V., Stockdon, H. F., Long, J. W., Guy, K., Thompson, D. M., et al. (2014). Channel networks within lava flows: Formation, evolution, and implications for flow behavior. *Journal of Geophysical Research: Earth Surface*, *119*(2), 1704–1724. https://doi.org/10.1002/2013JF002871

Dietterich, H. R., Diefenbach, A. K., Soule, S. A., Zoeller, M. H., Patrick, M. P., Major, J. J., & Lundgren, P. R. (2021). Lava effusion rate evolution and erupted volume during the 2018 Kīlauea lower East Rift Zone eruption. *Bulletin of Volcanology*, *83*(4), 25. https://doi.org/10.1007/s00445-021-01443-6

Dvigalo, V. N., Melekestsev, I. V., Shevchenko, A. V., & Svirid, I. Y. (2013). The 2010-2012 eruption of Kizimen Volcano: The greatest output (from the data of remote-sensing observations) for eruptions in Kamchatka in the early 21st century part I. The November 11, 2010 to December 11, 2011 phase. *Journal of Volcanology and Seismology*, *7*(6), 345–361. https://doi.org/10.1134/S074204631306002X

Fergason, R. L., Hare, T. M., & Laura, J. (2018). *HRSC and MOLA blended digital elevation model at 200m v2, astrogeology PDS annex*. US Geological Survey.

Filiberto, J. (2017). Geochemistry of Martian basalts with constraints on magma Genesis. *Chemical Geology*, *466*(June), 1–14. https://doi.org/10.1016/j.chemgeo.2017.06.009

Flynn, I. (2022). PyFLOWGO data for Arsia Mons lava flows. https://doi.org/10.5281/ZENODO.6985595

Flynn, I. T. W., Crown, D. A., & Ramsey, M. S. (2021). The effects of DEM resolution on planetary thermo-rheological lava flow modeling. In *52nd Lunar and Planetary Science Conference* (p. 1305).

Ganci, G., Cappello, A., Bilotta, G., & del Negro, C. (2020). How the variety of satellite remote sensing data over volcanoes can assist hazard monitoring efforts: The 2011 eruption of Nabro volcano. *Remote Sensing of Environment*, *236*, 111426. https://doi.org/10.1016/j.rse.2019.111426

Garry, W., Williams, D., & Bleacher, J. (2014). Geologic mapping of Arsia and Pavonis Montes, Mars. In *Lunar and Planetary Science Conference* (p. 2133).

Garry, W. B., Zimbelman, J. R., & Gregg, T. K. P. (2007). Morphology and emplacement of a long channeled lava flow near Ascraeus Mons Volcano, Mars. *Journal of Geophysical Research: Planets*, *112*(8), 1–21. https://doi.org/10.1029/2006JE002803

Giacomini, L., Carli, C., Sgavetti, M., & Massironi, M. (2012). Spectral analysis and geological mapping of the Daedalia Planum lava field (Mars) using OMEGA data. *Icarus*, *220*(2), 679–693. https://doi.org/10.1016/j.icarus.2012.06.010

Giordano, D., Russell, J. K., & Dingwell, D. B. (2008). Viscosity of magmatic liquids: A model. *Earth and Planetary Science Letters*, *271*(1–4), 123–134. https://doi.org/10.1016/j.epsl.2008.03.038

Glaze, L. S., & Baloga, S. M. (2006). Rheologic inferences from the levees of lava flows on Mars. *Journal of Geophysical Research: Planets*, *111*(9), 1–10. https://doi.org/10.1029/2005JE002585

Glaze, L. S., & Baloga, S. M. (2007). Topographic variability on Mars: Implications for lava flow modeling. *Journal of Geophysical Research: Planets*, *112*(8), 1–9. https://doi.org/10.1029/2006JE002879

Glaze, L. S., Baloga, S. M., Brent Garry, W., Fagents, S. A., & Parcheta, C. (2009). A hybrid model for leveed lava flows: Implications for eruption styles on Mars. *Journal of Geophysical Research: Planets*, *114*(7), 1–15. https://doi.org/10.1029/2008JE003278

Greeley, R., & Spudis, P. D. (1981). Volcanism on Mars. *Reviews of Geophysics and Space Physics*, *19*(5839), 13–41. https://doi.org/10.1038/294305a0

Gregg, T. K. P., & Fink, J. H. (1996). Quantification of extraterrestrial lava flow effusion rates through laboratory simulations. *Journal of Geophysical Research: Planets*, *101*(E7), 16891–16900. https://doi.org/10.1029/96JE01254

Griffiths, R. W., & Fink, J. H. (1992). The morphology of lava flows in planetary environments: Predictions from analog experiments. *Journal of Geophysical Research*, *97*(B13), 739–748. https://doi.org/10.1029/92jb01953

Harris, A., Chevrel, M., Coppola, D., Ramsey, M., Hrysiewicz, A., Thivet, S., et al. (2019). Validation of an integrated satellite-data-driven response to an effusive crisis: The April–may 2018 eruption of Piton de la Fournaise. *Annals of GeophysicsAnnals of Geophysics*, *61*(2018). https://doi.org/10.4401/ag-7972

Harris, A., Favalli, M., Mazzarini, F., & Pareschi, M. T. (2007). Best-fit results from application of a thermo-rheological model for channelized lava flow to high spatial resolution morphological data. *Geophysical Research Letters*, *34*(1), 1–5. https://doi.org/10.1029/2006GL028126

Harris, A., Murray, J. B., Aries, S. E., Davies, M. A., Flynn, L. P., Wooster, M. J., et al. (2000). Effusion rate trends at Etna and Krafla and their implications for eruptive mechanisms. *Journal of Volcanology and Geothermal Research*, *102*(3–4), 237–269. https://doi.org/10.1016/S0377-0273(00)00190-6

Harris, A., & Rowland, S. K. (2001). FLOWGO: A kinematic thermo-rheological model for lava cooling in A channel. *Bulletin of Volcanology*, *63*(1), 20–44. https://doi.org/10.1007/s004450000120

Harris, A., & Rowland, S. K. (2015). FLOWGO 2012, an updated framework for thermorheological simulations of channel-contained lava. *Hawaiian Volcanoes: From Source to Surface, Geophysical Monograph Series*, *208*, 457–481.

Harris, A. J. L., Rhéty, M., Gurioli, L., Villeneuve, N., & Paris, R. (2016). Simulating the thermorheological evolution of channel-contained lava: FLOWGO and its implementation in EXCEL. *Geological Society - Special Publications*, *426*(1), 313–336. https://doi.org/10.1144/SP426.9

Hauber, E., Bleacher, J., Gwinner, K., Williams, D., & Greeley, R. (2009). The topography and morphology of low shields and associated landforms of plains volcanism in the Tharsis region of Mars. *Journal of Volcanology and Geothermal Research*, *185*(1–2), 69–95. https://doi.org/10.1016/j.jvolgeores.2009.04.015

Hauber, E., Bro, P., Jagert, F., Jod, P., & Platz, T. (2011). Very recent and wide - spread basaltic volcanism on Mars. *Geophysical Research Letters*, *38*(10), 1–5. https://doi.org/10.1029/2011GL047310

Hiesinger, H., Head, J., & Neukum, G. (2007). Young lava flows on the eastern flank of Ascraeus mons: Rheological properties derived from high resolution Stereo camera (HRSC) images and Mars orbiter laser altimeter (MOLA) data. *Journal of Geophysical Research: Planets*, *112*(5), E05011. https://doi.org/10.1029/2006JE002717

Hodges, C. A., & Moore, H. J. (1994). *Atlas of volcanic landforms on Mars*. US Government Printing Office.

Hon, K., Kauahikaua, J., Denlinger, R., & Mackay, K. (1994). Emplacement and inflation of pahoehoe sheet flows: Observations and measurements of active lava flows on Kilauea volcano, Hawaii. *The Geological Society of America Bulletin*, *106*(3), 351–370. https://doi.org/10.1130/0016-7606(1994)106<0351:EAIOPS>2.3.CO;2

Hulme, G. (1976). The determination of the rheological properties and effusion rate of an Olympus Mons lava. *Icarus*, *27*(2), 207–213. https://doi.org/10.1016/0019-1035(76)90004-X

Kerr, R. C., Griffiths, R. W., & Cashman, K. V. (2006). Formation of channelized lava flows on an unconfined slope. *Journal of Geophysical Research*, *111*(10), 1–13. https://doi.org/10.1029/2005JB004225

Kienzle, S. (2004). The effect of DEM raster resolution on first order, second order and compound terrain derivatives. *Transactions in GIS*, *8*(1), 83–111. https://doi.org/10.1111/j.1467-9671.2004.00169.x

Kolzenburg, S., Jaenicke, J., Münzer, U., & Dingwell, D. B. (2018). The effect of inflation on the morphology-derived rheological parameters of lava flows and its implications for interpreting remote sensing data - a case study on the 2014/2015 eruption at Holuhraun, Iceland. *Journal of Volcanology and Geothermal Research*, *357*, 200–212. https://doi.org/10.1016/j.jvolgeores.2018.04.024

Kubanek, J., Westerhaus, M., & Heck, B. (2017). TanDEM-X time series analysis reveals lava flow volume and effusion rates of the 2012–2013 Tolbachik, Kamchatka fissure eruption. *Journal of Geophysical Research: Solid Earth*, *122*(10), 7754–7774. https://doi.org/10.1002/2017JB014309

Lang, N. P., Tornabene, L. L., McSween, H. Y., & Christensen, P. R. (2009). Tharsis-sourced relatively dust-free lavas and their possible relationship to Martian meteorites. *Journal of Volcanology and Geothermal Research*, *185*(1–2), 103–115. https://doi.org/10.1016/j.jvolgeores.2008.12.014

Lee, R. J., & Ramsey, M. S. (2016, December). What is the emissivity of active basaltic lava flows. In *Proceedings of the AGU Fall Meeting, San Francisco, CA, USA* (pp. 12–16).

Lipman, P. W., & Banks, N. (1987). A'a flow dynamics, 1984 Mauna Loa eruption. *Volcanism in Hawaii*, *43*.

Lopes, R. M., & Kilburn, C. R. (1990). Emplacement of lava flow fields: Application of terrestrial studies to Alba Patera, Mars. *Journal of Geophysical Research*, *95*(B9), 14383–14397. https://doi.org/10.1029/jb095ib09p14383

Malin, M. C. (2007). *MRO Context Camera experiment data record level 0 V1.0, MRO-M-CTX-2-EDR-L0-V1.0*. NASA Planetary Data System. https://doi.org/10.17189/1520266

Malin, M. C., Bell, J. F., Cantor, B. A., Caplinger, M. A., Calvin, W. M., Clancy, R. T., et al. (2007). Context camera investigation on board the Mars reconnaissance orbiter. *Journal of Geophysical Research: Planets*, *112*(5), 1–25. https://doi.org/10.1029/2006JE002808

McEwen, A. (2007). Mars reconnaissance orbiter high resolution imaging science experiment, reduced data record, MRO-M-HIRISE-3-RDR-V1.1, NASA Planetary Data System. https://doi.org/10.17189/1520303

Mouginis-Mark, P., Rowland, S., & Wilson, L. (2022). Planetary volcanism: Craters, lava flows, fissures, and insights into their formation from observations of the April–August 2018 eruption of Kīlauea Volcano, Hawai'i. In *Planetary volcanism across the solar system* (pp. 77–114). Elsevier.

Mouginis-Mark, P., & Yoshioka, M. T. (1998). The long lava flows of Elysium Planita, Mars. *Journal of Geophysical Research*, *103*(E8), 19389–19400. https://doi.org/10.1029/98je01126

Mouginis-Mark, P. J., & Rowland, S. K. (2008). Lava flows at Arsia mons, Mars: Insights from a graben imaged by HiRISE. *Icarus*, *198*(1), 27–36. https://doi.org/10.1016/j.icarus.2008.06.015

Pasckert, J. H., Hiesinger, H., & Reiss, D. (2012). Rheologies and ages of lava flows on Elysium Mons, Mars. *Icarus*, *219*(1), 443–457. https://doi.org/10.1016/j.icarus.2012.03.014

Patrick, M. R., Dietterich, H. R., Lyons, J. J., Diefenbach, A. K., Parcheta, C., Anderson, K. R., et al. (2019). Cyclic lava effusion during the 2018 eruption of Kīlauea Volcano. *Science*, *366*(6470). https://doi.org/10.1126/science.aay9070

Peitersen, M., & Crown, D. A. (1999). Downflow width behavior of Martian and terrestrial lava flows. *Journal of Geophysical Research*, *104*(E4), 8473–8488. https://doi.org/10.1029/1999je900003

Peters, S. I., Christensen, P. R., & Clarke, A. B. (2021). Lava flow eruption conditions in the Tharsis volcanic province on Mars. *Journal of Geophysical Research: Planets*, *126*, e2020JE006791. https://doi.org/10.1029/2020JE006791

Plechov, P., Blundy, J., Nekrylov, N., Melekhova, E., Shcherbakov, V., & Tikhonova, M. S. (2015). Petrology and volatile content of magmas erupted from Tolbachik Volcano, Kamchatka, 2012-13. *Journal of Volcanology and Geothermal Research*, *307*, 182–199. https://doi.org/10.1016/j.jvolgeores.2015.08.011

Plescia, J. B. (2004). Morphometric properties of Martian volcanoes. *Journal of Geophysical Research: Planets*, *109*(3), 1–26. https://doi.org/10.1029/2002je002031

Ramsey, M. S., Chevrel, M. O., Coppola, D., & Harris, A. J. L. (2019). The influence of emissivity on the thermo-rheological modeling of the channelized lava flows at tolbachik volcano. *Annals of Geophysics*, *62*(2). https://doi.org/10.4401/ag-8077

Rhéty, M., Harris, A., Villeneuve, N., Gurioli, L., Médard, E., Chevrel, O., & Bachélery, P. (2017). A comparison of cooling-limited and volume-limited flow systems: Examples from channels in the Piton de la Fournaise April 2007 lava-flow field. *Geochemistry, Geophysics, Geosystems*, *18*(9), 3270–3291. https://doi.org/10.1002/2017GC006839

Richardson, J. A., Bleacher, J. E., Connor, C. B., & Glaze, L. S. (2021). Small volcanic vents of the Tharsis volcanic province, Mars. *Journal of Geophysical Research: Planets*, *126*(2), 1–23. https://doi.org/10.1029/2020JE006620

Richardson, J. A., Wilson, J. A., Connor, C. B., Bleacher, J. E., & Kiyosugi, K. (2017). Recurrence rate and magma effusion rate for the latest volcanism on Arsia Mons, Mars. *Earth and Planetary Science Letters*, *458*, 170–178. https://doi.org/10.1016/j.epsl.2016.10.040

Rowland, S. K., Garbeil, H., & Harris, A. J. L. (2005). Lengths and hazards from channel-fed lava flows on Mauna Loa, Hawai'i, determined from thermal and downslope modeling with FLOWGO. *Bulletin of Volcanology*, *67*(7), 634–647. https://doi.org/10.1007/s00445-004-0399-x

Rowland, S. K., Harris, A. J. L., & Garbeil, H. (2004). Effects of Martian conditions on numerically modeled, cooling-limited, channelized lava flows. *Journal of Geophysical Research: Planets*, *109*(10), 1–16. https://doi.org/10.1029/2004JE002288

Rowland, S. K., Harris, A. J. L., & Kallianpur, K. (2002). Vent locations on elysium mons, Mars, from thermal modeling of lava flows. *LPSC*, *33*, 1441.

Ruff, S. W., & Christensen, P. R. (2002). Bright and dark regions on Mars: Particle size and mineralogical characteristics based on thermal emission spectrometer data. *Journal of Geophysical Research: Planets*, *107*(12), 1–22. https://doi.org/10.1029/2001je001580

Russo, F. P., Flynn, I. T. W., & Ramsey, M. S. (2022). The impact of slope variability on the modeling of Martian lava flows. *LPI Contribution*, *2678*, 1410.

Ryerson, F. J., Weed, H. C., & Piwinskii, A. J. (1988). Rheology of subliquidus magmas. 1. Picritic compositions. *Journal of Geophysical Research*, *93*(B4), 3421–3436. https://doi.org/10.1029/JB093iB04p03421

Sautter, V., Toplis, M. J., Wiens, R. C., Cousin, A., Fabre, C., Gasnault, O., et al. (2015). In situ evidence for continental crust on early Mars. *Nature Geoscience*, *8*(8), 605–609. https://doi.org/10.1038/ngeo2474

Scott, D. H., & Tanaka, K. L. (1986). Geologic map of the western equatorial region of Mars, scale 1:15,000,000. U.S. Geological survey map I-1802-A. Retrieved from http://astrogeology.usgs.gov/Projects/PlanetaryMapping/DIGGEOL/mars/marswest/mw.pdf%5Cnpapers3://publication/uuid/9DE8930B-BC79-41A2-98E9-42D39A4380EF

Scott, D. H., & Zimbelman, J. R. (1995). Geologic map of Arsia Mons volcano, Mars.

Simurda, C. M., Ramsey, M. S., & Crown, D. A. (2019). The unusual thermophysical and surface properties of the daedalia planum lava flows. *Journal of Geophysical Research: Planets*, *124*(7), 1945–1959. https://doi.org/10.1029/2018JE005887

Smith, D., Neumann, G., Arvidson, R. E., Guinness, E. A., & Slavney, S. (2003). *Mars Global Surveyor laser altimeter mission experiment gridded data record*. NASA Planetary Data System.

Soldati, A., Houghton, B. F., & Dingwell, D. B. (2021). A lower bound on the rheological evolution of magmatic liquids during the 2018 Kilauea eruption. *Chemical Geology*, *576*, 120272. https://doi.org/10.1016/j.chemgeo.2021.120272

Sparks, R. S. J., Pinkerton, H., & Hulme, G. (1976). Classification and formation of lava levees on mount Etna, Sicily. *Geology*, *4*(5), 269–271. https://doi.org/10.1130/0091-7613(1976)4<269:cafoll>2.0.co;2

Tanaka, K. L., Robbins, S. J., Fortezzo, C. M., Skinner, J. A., & Hare, T. M. (2014). The digital global geologic map of Mars: Chronostratigraphic ages, topographic and crater morphologic characteristics, and updated resurfacing history. *Planetary and Space Science*, *95*, 11–24. https://doi.org/10.1016/j.pss.2013.03.006

Thompson, J. O., & Ramsey, M. S. (2021). The influence of variable emissivity on lava flow propagation modeling. *Bulletin of Volcanology*, *83*(6), 1–19. https://doi.org/10.1007/s00445-021-01462-3

Vaucher, J., Baratoux, D., Toplis, M. J., Pinet, P., Mangold, N., & Kurita, K. (2009). The morphologies of volcanic landforms at Central Elysium Planitia: Evidence for recent and fluid lavas on Mars. *Icarus*, *200*(1), 39–51. https://doi.org/10.1016/j.icarus.2008.11.005

Volynets, A. O., Edwards, B. R., Melnikov, D., Yakushev, A., & Griboedova, I. (2015). Monitoring of the volcanic rock compositions during the 2012–2013 fissure eruption at Tolbachik volcano, Kamchatka. *Journal of Volcanology and Geothermal Research*, *307*, 120–132.

Wantim, M. N., Kervyn, M., Ernst, G. G. J., del Marmol, M. A., Suh, C. E., & Jacobs, P. (2013). Numerical experiments on the dynamics of channelised lava flows at Mount Cameroon volcano with the FLOWGO thermo-rheological model. *Journal of Volcanology and Geothermal Research*, *253*, 35–53. https://doi.org/10.1016/j.jvolgeores.2012.12.003

Warner, N. H., & Gregg, T. K. P. (2003). Evolved lavas on Mars? Observations from southwest Arsia mons and Sabancaya volcano, Peru. *Journal of Geophysical Research: Planets*, *108*(10), 5112. https://doi.org/10.1029/2002je001969

Wechsler, S. F., & Kroll, C. N. (2006). Quantifying DEM uncertainty and its effect on topographic parameters. *Photogrammetric Engineering & Remote Sensing*, *72*(9), 1081–1090. https://doi.org/10.14358/PERS.72.9.1081

Wilson, L., & Head, J. W. (1983). A comparison of volcanic eruption processes on Earth, Moon, Mars, Io and Venus. *Nature*, *302*(5910), 663–669. https://doi.org/10.1038/302663a0

Wilson, L., & Mouginis-Mark, P. J. (2001). Estimation of volcanic eruption conditions for a large flank event on Elysium Mons, Mars. *Journal of Geophysical Research*, *106*(E9), 20621–20628. https://doi.org/10.1029/2000je001420

Zimbelman, J. (1985). Estimates of rheologic properties for flows on the Martian volcano Ascraeus Mons. *Journal of Geophysical Research*, *90*(S01), 157. https://doi.org/10.1029/jb090is01p00157

Zimbelman, J. R. (1998). Emplacement of long lava flows on planetary surfaces. *Journal of Geophysical Research*, *103*(B11), 27503–27516. https://doi.org/10.1029/98jb01123

Zimbelman, J. R., & McAllister, R. (1985). Surface morphology on the Martian volcano Ascraeus mons. In *Lunar and Planetary Science Conference* (Vol. *16*, pp. 936–937).